Diffraction Tomography of the Disturbed Ionosphere Based on GPS Scintillation Data

by Mark L. Psiaki
Cornell University, Ithaca, N.Y., 14853-7501, U.S.A.

Gary S. Bust
ASTRA, 12703 Spectrum Drive Suite 101, San Antonio, Texas 78249, U.S.A.

Alessandro P. Cerruti, Paul M. Kintner, Jr., and Steven P. Powell
Cornell University, Ithaca, N.Y. 14853-7501, U.S.A

BIOGRAPHIES

Mark L. Psiaki is a Professor in the Sibley School of Mechanical and Aerospace Engineering. He received a B.A. in Physics and M.A. and Ph.D. degrees in Mechanical and Aerospace Engineering from Princeton University. His research interests are in the areas of estimation and filtering, spacecraft attitude and orbit determination, and GNSS technology and applications.

Gary S. Bust received his Ph.D. in Physics in 1989 from the University of Texas at Austin and currently is a senior research scientist for Atmospheric and Space Technology Research Associates. His areas of interest include ionospheric tomographic imaging, data assimilation, and the application of space based observations to ionospheric remote sensing.

Alessandro P. Cerruti is a 2008 Ph.D. graduate of the Space Physics and Engineering Group in the School of Electrical and Computer Engineering. He currently works for the MITRE Corporation. One of his primary interests is space weather and its effects on GNSS receiver operation.

Paul M. Kintner, Jr. is a Professor of Electrical and Computer Engineering. He received a B.S in Physics from the University of Rochester and a Ph.D. in Physics from the University of Minnesota. His research interests include the electrical properties of upper atmospheres, space weather, and developing GNSS instruments for space science. He is a Fellow of the APS.

Steven P. Powell is a Senior Engineer with the Space Plasma Physics Group in the Department of Electrical and Computer Engineering. He has M.S. and B.S. degrees in Electrical Engineering from Cornell University. He has been involved with the design, fabrication, and testing of several GNSS receivers.

ABSTRACT

A new inverse diffraction algorithm has been developed to estimate the fine-scale ionospheric electron density variations that cause equatorial scintillation in GPS signals. This work is part of an effort to image the disturbed ionosphere in order to better understand scintillation from a scientific standpoint. The new algorithm relies on a physical model of how electron density irregularities affect received GPS signals in ground-based receivers. The model is based on a thin phase-screen approximation of the ionosphere that accounts for non-normal incidence of the GPS signal. The heart of the model is a modified Huygens-Fresnel integral that is evaluated using FFT-based techniques. The forward model computes the received in-phase and quadrature accumulations as functions of a "frozen", drifting 1-dimensional vertical electron density profile. Inversion of this model is performed using nonlinear least-squares techniques. The final algorithm estimates electron density profiles based on measured accumulations from a dual-frequency GPS receiver. The algorithm has been applied to weak scintillation data. It has demonstrated an ability to fit dual-frequency amplitude and phase data based on a single electron density profile.

INTRODUCTION

Ionospheric scintillation is an important topic both technologically and scientifically. Scintillation is caused by irregularities in the ionosphere, and it appears as rapid amplitude or phase fluctuations, or a combination of the two, on radio frequency (RF) signals that traverse the ionosphere [1]. The present paper concentrates on equatorial scintillation, which occurs near the Earth's magnetic equator after local sunset at certain times of year [2]. Amplitude fades of 30 dB have been recorded during equatorial scintillation, and rapid phase changes

Preprint from ION GNSS 2008

tend to accompany these deep fades [3,4]. The rapid amplitude and phase dynamics tend to cause radio receivers to lose carrier lock [1,3,4], which makes scintillation a major problem for Global Navigation Satellite Systems (GNSS) and for trans-ionospheric radio communication.

The technological importance of the negative impacts of scintillation has given rise to scientific interest in understanding the physics of the ionospheric irregularities that cause scintillation. These irregularities are caused by electron density bubbles that can form due to Rayleigh-Taylor instability in an inversion that often occurs after local sunset [5]. Observational data have been used to study the statistical properties of these irregularities [6,7,8,9]. There remain, however, several important unknowns about these irregularities. Science cannot yet predict whether a given inversion will develop into the irregularities that cause scintillation, nor does it understand the detailed dynamics of how the bubbles form or how they give rise to irregularities which have length scales that cause scintillation.

The present study is the first result of an extensive effort to use remote sensing techniques in order to image the electron density variations that cause equatorial ionospheric scintillation. These techniques are being developed based on GPS data. The goal is to image the disturbed ionosphere based on distributed measurements of dual-frequency GPS amplitude and phase scintillation made by an array of ground-based receivers, as depicted in Fig. 1. This effort's principle goal is to produce a set of fine-scale electron density maps, or images, of the scintillating equatorial ionosphere. These maps will provide ionospheric physicists with valuable data from which they can deduce improved scintillation models. It is hoped that such models will lead to improved abilities to predict and monitor scintillation and to operate GNSS and RF communication equipment in their presence.

This first study has the limited goal of developing and testing an algorithm that computes a 1-dimensional electron density image of the scintillating ionosphere. It does this based on the scintillating signals from a single GPS satellite as received by a single ground-based dual-frequency GPS receiver. The limitation to one receiver and one satellite has been imposed by the currently available data [10], not by choice.

This paper makes 4 contributions to the subject of inverse diffraction imaging of the ionospheric irregularities that cause equatorial scintillation. The first is a phase-screen model of the effects of a 1-dimensional electron density distribution on the amplitude and phase variations of received RF signals at multiple frequencies. The new feature of this phase-screen model versus existing models (e.g., see Ref. 11), is its ability to deal with non-normal incidence of the RF signal on the plane of its ionospheric phase screen. The second contribution is a mathematical model of how the disturbed ionosphere affects the group delay. The third contribution is a model inversion algorithm that estimates the electron density irregularities along with other ionospheric parameters based on remotely sensed dual-frequency GPS receiver data. It does this by applying nonlinear least-squares techniques to an FFT-based implementation of the forward phase-screen calculation. The fourth contribution is the application of this model inversion algorithm to actual dual-frequency scintillation data and an evaluation of its effectiveness.

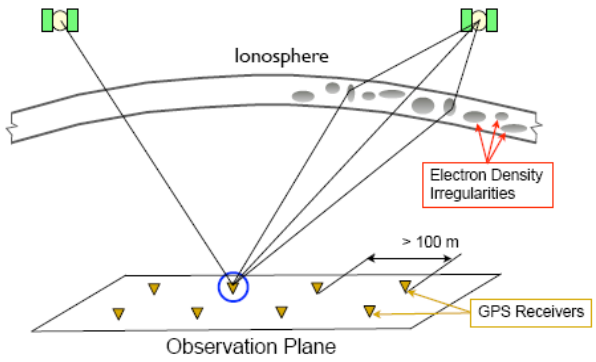

Fig. 1 Schematic diagram of a GPS remote-sensing array for inverse-diffraction imaging of the scintillating ionosphere [12].

The use of the word tomography in this paper's title is an unintended misnomer. The term tomography refers to a specific model inversion technique that passes probe signals through an unknown medium in two or more directions in order to make the characteristics of the medium observable. In the present context, the GNSS signal in question passes through the ionosphere primarily in a single direction, though satellite motion does cause slight directional variations. The present technique relies on the physics of diffraction in order to make the ionospheric electron density distribution observable. It does not rely on a multiplicity of signal directions. A better title would have been "Inverse Diffraction Imaging of the Disturbed Ionosphere based on GPS Scintillation Data." The current title has been used because this error was not realized until after the conference program had gone to press. In the future, this project hopes to use true tomography methods by fielding a distributed array of receivers which can track signals that pass through a given portion of the disturbed ionosphere in multiple directions.

The remainder of this paper consists of 4 main sections plus conclusions. Section II develops the ionospheric phase-screen model for a plane wave that can have non-normal incidence on the phase-screen plane. It defines the "frozen", drifting ionosphere assumption that is needed in order to process data from a single receiver, and it develops the FFT/inverse-FFT (IFFT) techniques

that are needed in order to perform its phase-screen calculations. Section III develops a phase-screen inverse diffraction algorithm that is based on the Gauss-Newton and Levenberg-Marquardt techniques for solving nonlinear least-squares problems. It also explains how the FFT and IFFT phase-screen calculations can be efficiently embedded in its least-squares algorithm. Section IV describes the collection and pre-processing of dual-frequency scintillation data that provide the inputs to the model inversion algorithm of Section III. Section V applies the inverse diffraction method of Section III to the data of Section IV and discusses the results. Section VI summarizes the main results and presents conclusions.

II. IONOSPHERIC PHASE-SCREEN MODEL WITH NON-NORMAL INCIDENCE

This section develops a mathematical model of how ionospheric electron density variations give rise to amplitude and phase scintillation at a receiver. The model used is a phase-screen model, like those described in Refs. 6 and 11. It models the ionosphere as a thin plane at which abrupt changes of carrier phase occur. The effects of these changes are propagated from the ionosphere to a ground-based GPS receiver by using a Huygens-Fresnel-type approximation of Kirchhoff's boundary integral. The present section develops a generalized phase-screen model that has two new features. One is the ability to model non-normal incidence of the RF plane wave on the phase-screen plane. The other is the ability to model the effect on group delay of the phase screen's electron density irregularities.

A. Phase-Screen Geometry with Non-Normal Incidence

The phase-screen models of Refs. 6 and 11 deal with the case of a plane wave whose direction of travel is exactly perpendicular to the phase-screen plane. The present paper needs to work with actual GPS data. The assumption of normal incidence is almost never true when using real data. Therefore, a generalized phase-screen model has been developed for the non-normal case.

The geometry associated with the generalized phase-screen model is depicted in Fig. 2. The ionospheric phase-screen plane is the x-y plane whose origin is defined to lie on the line of sight (LOS) between the receiver antenna and the nominal location of the GPS satellite that transmits the scintillating signals. Definition of the phase-screen origin relative to WGS-84 coordinates is completed by specification of its altitude h above the WGS-84 ellipsoid. This origin is denoted by the WGS-84 position vector $\boldsymbol{r}_{ppnom}$, with the "pp" subscript being shorthand for "pierce point".

The $+y$ axis of the phase-screen plane is defined to be aligned with the local International Geomagnetic Reference Field (IGRF) vector at the x-y origin, $\boldsymbol{B}(\boldsymbol{r}_{ppnom})$, which points approximately horizontal and approximately northward when near the magnetic equator. The $+x$ axis points approximately westward. The alignment of the $+x$ axis relative to local horizontal is defined by the ionospheric tilt angle γ. If $\gamma = 0$, then the $+x$ axis is exactly horizontal. If $\gamma \neq 0$, then the $+x$ axis is rotated about the $+y$ axis to make an angle of γ between it and the horizontal axis that is perpendicular to the y axis. $\gamma > 0$ causes an upward tilt of the $+x$ axis, and $\gamma < 0$ causes a downward tilt.

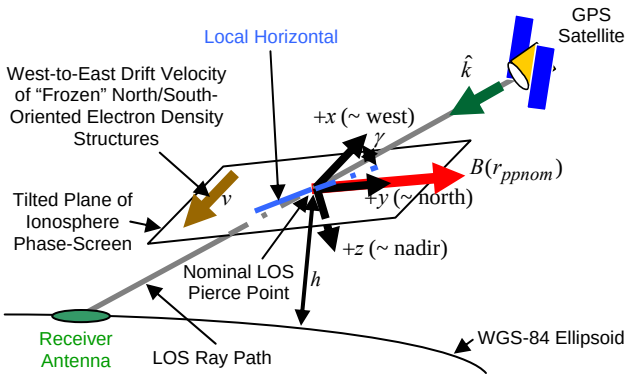

Fig. 2. Geometry of phase-screen model.

A non-zero ionospheric tilt is allowed because this possibility may be implied by the observations and analyses of Refs. 13 and 14. One goal of the present study is to try to estimate the tilt angle γ along with the altitude h.

The $+z$ axis of the phase-screen coordinate system is defined by the right-hand rule. It points approximately towards nadir.

Two additional geometric quantities of interest are the unit direction vector that points from the GPS spacecraft to the receiver antenna and the receiver antenna location. The unit-normalized LOS direction vector is $\hat{\boldsymbol{k}}(t) = [\,\hat{k}_1(t)\,;\hat{k}_2(t)\,;\hat{k}_3(t)\,]$, where $\hat{k}_i$ is its component along the i^{th} phase-plane axis, $i = 1$ referring to the x axis, $i = 2$ to the y axis, and $i = 3$ to the z axis. This vector is a function of time because of motion of the GPS satellite. The nominal LOS direction vector applies at time t_{nom} and is given by $\hat{\boldsymbol{k}}(t_{nom}) = \hat{\boldsymbol{k}}_0 = [\,\hat{k}_{10}\,;\hat{k}_{20}\,;\hat{k}_{30}\,]$. The receiver antenna location can be defined in terms of this vector and z_a, the antenna's z coordinate: $\boldsymbol{r}_a = z_a[(\hat{k}_{10}/\hat{k}_{30})\,;(\hat{k}_{20}/\hat{k}_{30})\,;1]$. Note that $\hat{k}_{30} > 0$ and $\hat{k}_3(t) > 0$ are typical and that $\hat{k}_{10}^2 + \hat{k}_{20}^2 + \hat{k}_{30}^2 = \hat{k}_1^2(t) + \hat{k}_2^2(t) + \hat{k}_3^2(t) = 1$ due to the unit normalization constraint. The quantities $\hat{k}_1(t)$, $\hat{k}_2(t)$, $\hat{k}_3(t)$, $\hat{k}_{10}$, $\hat{k}_{20}$, $\hat{k}_{30}$, and z_a all depend on the altitude h and the tilt angle γ because h and γ determine the location and orientation of the ionospheric coordinate system relative to the antenna

and the GPS spacecraft.

B. Modeling Electron Density Variations and their Phase Effects

The phase-screen scintillation calculations use a modeled electron density distribution in the *x*-*y* plane in order to determine the phase increment that occurs as an RF signal crosses that plane. This density model takes the general form $VTEC(x,y,t)$, where *VTEC* stands for vertical total electron content in electrons/m^2. The designation "vertical" is not quite accurate. This density profile actually gives the number of electrons in a 1m-by-1m column that projects perpendicular from the phase-screen plane in the +/- *z* direction, which normally is not exactly equal to true vertical.

There is strong evidence that ionospheric irregularities that cause equatorial scintillation are elongated in the direction of the local magnetic field, i.e., in the *y* direction [13]. This observation implies that the electron density does not vary strongly in the *y* direction. Therefore, its *y* dependence has been neglected, and the functional form of the distribution has been approximated as $VTEC(x,t)$.

Another observed property of equatorial scintillation is that the irregularities tend to drift from west to east much faster than they tend to deform relative to this drifting reference frame [13]. Therefore, it might be reasonable to model the joint spatial/temporal dependence of the "vertical" electron density distribution in the form $VTEC(x+v[t-t_0])$, where $VTEC(x)$ is the distribution at time $t = t_0$ and where v is the west-to-east drift velocity of the electron density irregularities. This drift velocity is depicted in Fig. 2.

The $VTEC(x+v[t-t_0])$ form of the $VTEC(x,t)$ model is called a "frozen", drifting distribution. It is the model that is used throughout the remainder of this paper. The decision to use this model form has been made because there is evidence that it is reasonable [13] and because it limits the number of unknowns. If the distribution $VTEC(x,t)$ were allowed to deform with respect to itself as well as drift, then it is likely that many more GPS receivers would be needed in order to make this distribution observable. It is hoped that additional receivers will be fielded in future scintillation data collection campaigns so that their outputs will enable relaxation of this assumption of a "frozen", drifting 1-dimensional *VTEC* distribution.

There is evidence that the scintillation region can have a non-zero vertical descent rate [14]. This possibility that h is a function of time is not permitted in the current phase-screen model. Again, the reason for not including this possibility is the increased likelihood that the resulting system would not yield a unique best-fit solution to dual-frequency data from a single GPS receiver. It is hoped that this restriction can be relaxed when dual-frequency scintillation data are available from a receiver array.

Given $VTEC(x+v[t-t_0])$, the phase change that occurs at the phase screen can be determined from the usual phase advance formula [15]:

$$\Delta\phi(x,t) = \frac{\Delta\bar{\phi}(x+v[t-t_0])}{\hat{k}_3(t)} = (2\pi)^2\left[\frac{40.3\,VTEC(x+v[t-t_0])}{c\omega}\right]\frac{1}{\hat{k}_3(t)} \quad (1)$$

where $\Delta\phi(x,t)$ is the carrier phase advance in radians, $\Delta\bar{\phi}(x+v[t-t_0])$ is the phase advance that would have occurred if the RF plane wave's incidence had been normal to the phase-screen plane, $1/\hat{k}_3(t)$ is the non-normal-incidence slant factor that converts *VTEC* to *TEC*, c is the speed of light, and ω is the carrier frequency in radians/sec.

The phase increment in Eq. (1) can be combined with the incident plane wave model to yield a formula for any relevant signal quantity. Suppose that $u(x,y,z,t)$ is the quantity of interest. It might be the signal voltage in the direction that is perpendicular to $\hat{\boldsymbol{k}}_0$ and to the *x* axis. If its value just above the phase-screen plane is the real part of

$$u(x,y,0^-,t) = A_0 \exp\left(j\omega\{t - \frac{\hat{\boldsymbol{k}}^{\mathrm{T}}(t)}{c}[\begin{bmatrix} x \\ y \\ 0 \end{bmatrix} - \boldsymbol{r}_{\boldsymbol{sc}}(t)]\}\right) \quad (2)$$

then its value just below the phase screen is the real part of

$$u(x,y,0^+,t) = A_0 \exp\left(j\Delta\phi(x,t) + j\omega\{t - \frac{\hat{\boldsymbol{k}}^{\mathrm{T}}(t)}{c}[\begin{bmatrix} x \\ y \\ 0 \end{bmatrix} - \boldsymbol{r}_{\boldsymbol{sc}}(t)]\}\right) \quad (3)$$

where A_0 is the signal amplitude above the phase screen and $\boldsymbol{r}_{sc}(t)$ is the location of the GPS spacecraft given in Cartesian phase-screen coordinates.

C. Non-Normal Huygens-Fresnel Propagation of Phase-Screen Model

A physics-based propagation is used to translate the signal in Eq. (3) from the bottom of the ionosphere to the receiver antenna. An exact form of this propagation can be implemented using Kirchhoff's boundary integral [16] if one assumes that that the ionospheric plane is of infinite extent and that there is no reflection of the wave from the ground. This propagation takes the form

$$u_a(t) = \frac{A_0}{4\pi} e^{j\omega[t-\tau_{na}(t)]} \int_{-\infty}^{\infty} dx \int_{-\infty}^{\infty} dy \times$$
$$\exp\left(j\Delta\phi(x,t) - j\frac{\omega}{c}\{\hat{\mathbf{k}}^{\mathrm{T}}(t)[\begin{bmatrix} x \\ y \\ 0 \end{bmatrix} - \mathbf{r_{sc}}(t)] + \rho_{ap}(x,y)\} \right) \times$$
$$\left(j\frac{\omega}{c}\left[\frac{\hat{k}_3(t)}{\rho_{ap}(x,y)} + \frac{z_a}{\rho_{ap}^2(x,y)} \right] + \frac{z_a}{\rho_{ap}^3(x,y)} \right) \qquad (4)$$

where $u_a(t)$ is the complex phasor form of the signal at the receiver antenna location, $z_a[(\hat{k}_{10}/\hat{k}_{30});(\hat{k}_{20}/\hat{k}_{30});1]$, $\tau_{na}(t)$ is the added signal delay due to the troposphere, and

$$\rho_{ap}(x,y) = \sqrt{(x - z_a\frac{\hat{k}_{10}}{\hat{k}_{30}})^2 + (y - z_a\frac{\hat{k}_{20}}{\hat{k}_{30}})^2 + z_a^2} \qquad (5)$$

is the distance from the receiver antenna to the ionospheric phase-screen location (x,y).

The last term in Eq. (4) the $z_a/\rho_{ap}{}^3$ term, is the near-field term. It is typically negligible in comparison to the other terms because ρ_{ap} is on the order of 300 km or more for typical ionospheric scintillation altitudes, whereas c/ω is typically on the order 0.04 m/rad or less for the L-band GPS signals that are considered in this study.

A Huygens-Fresnel-type approximation has been used in order to develop an alternative form of Eq. (4) that is amenable to FFT-based calculations. After neglecting the near-field term, the equation is approximated by a Taylor series in y expanded about the value of y that minimizes the exponential argument in the integrand. This minimizing value is a function of x. It is

$$y_{minarg}(x,t) = z_a\frac{\hat{k}_{20}}{\hat{k}_{30}} - \frac{\hat{k}_2(t)}{\sqrt{\hat{k}_1^2(t) + \hat{k}_3^2(t)}}\sqrt{(x - z_a\frac{\hat{k}_{10}}{\hat{k}_{30}})^2 + z_a^2} \qquad (6)$$

The exponential argument is expanded to second order in $\Delta y = y - y_{minarg}$, and the coefficient of the exponential is expanded to first order to in Δy. The integral with respect to y can then be carried out. The result is expanded in a Taylor series about the value of x that minimizes the remaining exponential argument terms aside from the $\Delta\phi(x,t)$ term. That minimizing value is

$$x_{minarg}(t) = z_a\left(\frac{\hat{k}_{10}}{\hat{k}_{30}} - \frac{\hat{k}_1(t)}{\hat{k}_3(t)} \right) \qquad (7)$$

The exponential argument terms other than the $\Delta\phi(x,t)$ term are expanded to second order in $\Delta x = x - x_{minarg}$, and the coefficient of the exponential is expanded to first order to in Δx. The resulting approximate formula for the received signal is

$$u_a(t) = A_s(t)e^{j\{\phi_s(t) + \omega[t - \rho_{asc}(t)/c - \tau_{na}(t)]\}} \qquad (8)$$

where $\rho_{asc}(t)$ is the distance from the GPS spacecraft to the receiver antenna. The quantities $A_s(t)$ and $\phi_s(t)$ are, respectively, the scintillating amplitude and phase of the received signal. They are evaluated using the following generalization of the Huygens-Fresnel integral to this section's model of non-normal incidence:

$$A_s(t)e^{j\phi_s(t)} = A_0\sqrt{\frac{j\psi(t)}{2\pi}} \int_{-\infty}^{\infty} [1 + \Delta x\zeta(t)] \times e^{j\{\Delta\bar{\phi}[\Delta x + x_{pv}(t)]/\hat{k}_3(t) - \frac{1}{2}\psi(t)\Delta x^2\}} d\Delta x \qquad (9)$$

where

$$\psi(t) = \omega\hat{k}_3^3(t)/\{cz_a[\hat{k}_1^2(t) + \hat{k}_3^2(t)]\} \qquad (10a)$$

$$\zeta(t) = [\hat{k}_1(t)\hat{k}_3(t)]/\{z_a[\hat{k}_1^2(t) + \hat{k}_3^2(t)]\} \qquad (10b)$$

$$x_{pv}(t) = v(t - t_0) + \{[\hat{k}_{10}/\hat{k}_{30}] - [\hat{k}_1(t)/\hat{k}_3(t)]\}z_a \qquad (10c)$$

Note that $x_{pv}(t)$ effectively gives the drifted x location of the LOS ionospheric pierce point as measured relative to the original "frozen" $VTEC(x)$ vs. x distribution.

The integral in Eq. (9) reduces to the standard normal-incidence Huygens-Fresnel integral for a 1-dimensional phase screen [6,11] under the right conditions. These conditions are that $\hat{k}_{10} = \hat{k}_1(t) = 0$ and that $\hat{k}_{30} = \hat{k}_3(t) = 1$. In this case, the formulas in Eqs. (10a)-(10c) simplify to $\psi = \omega/(cz_a)$, $\zeta = 0$, and $x_{pv}(t) = v(t\text{-}t_0)$.

D. FFT-Based Numerical Evaluation of Huygens-Fresnel Integral

The integral in Eq. (9) can be evaluated by using Fourier Transform techniques. Like the technique of Ref. 11, this approach relies on the convolution property of the Fourier transform and on the Fourier transform pair:

$$[1 + \eta\mu(t)]\frac{1}{\sqrt{j\psi(t)}}e^{j\frac{1}{2}\eta^2/\psi(t)} = \frac{1}{\sqrt{2\pi}}\int_{-\infty}^{\infty}[1 - \Delta x\zeta(t)]e^{-j\frac{1}{2}\psi(t)\Delta x^2}e^{-j\eta\Delta x}d\Delta x \qquad (11)$$

where η is the independent spatial frequency variable of the Fourier transform and where

$$\mu(t) = \zeta(t)/\psi(t) = \hat{k}_1(t)c/[\omega\hat{k}_3^2(t)] \qquad (12)$$

The convolution property of the Fourier transform states that the Fourier transform of the convolution of two functions is the product of the two functions' Fourier transforms. This property is applied to Eq. (9). If one introduces a sign change in the dummy integration variable Δx, then the integral in Eq. (9) is equivalent to a

convolution of the function $\exp\{j\Delta\bar{\phi}(\Delta x)/\hat{k}_3(t)\}$ with the integrand on the right-hand side of Eq. (11). $x_{pv}(t)$ is the independent variable in this convolution form of Eq. (9). Therefore, Eq. (9) can be re-written in the form

$$A_s(t)e^{j\phi_s(t)} = \frac{A_0}{\sqrt{2\pi}}\int_{-\infty}^{\infty} f(\eta,t)[1+\eta\mu(t)]e^{j\frac{1}{2}\eta^2/\psi(t)}e^{j\eta x_{pv}(t)}d\eta \quad (13)$$

where

$$f(\eta,t) = \frac{1}{\sqrt{2\pi}}\int_{-\infty}^{\infty} e^{j\Delta\bar{\phi}(\Delta x)/\hat{k}_3(t)}e^{-j\eta\Delta x}d\Delta x \quad (14)$$

The formulas in Eqs. (13) and (14) become practical if one uses FFT techniques in order to numerically evaluate their integrals. The use of such techniques implies two assumptions about the complex form of the phase-screen distribution $\exp\{j\Delta\bar{\phi}(\Delta x)/\hat{k}_3(t)\}$. The first assumption presumes that the signal is band-limited to less than half the sampling frequency of the FFT calculations. That is, if the FFT calculations use the phases at grid points $\Delta\bar{\phi}_i = \Delta\bar{\phi}(i\delta x)$ for i = 0, ..., (N-1), then the highest spatial frequency magnitude in $\exp\{j\Delta\bar{\phi}(\Delta x)/\hat{k}_3(t)\}$ is half the sampling frequency, $\eta_{max} = \pi/\delta x$. δx is the FFT grid spacing. The second assumption needed for FFT calculations is that $\Delta\bar{\phi}(\Delta x)$ is periodic with period equal to $N\delta x$: $\Delta\bar{\phi}(\Delta x) = \Delta\bar{\phi}(\Delta x + N\delta x)$ for all Δx.

Given these assumptions, Eq. (14) can be evaluated using the FFT formula

$$\bar{f}(n,t) = \sum_{i=0}^{N-1} e^{j\Delta\bar{\phi}([i-N/2]\delta x)/\hat{k}_3(t)}e^{-j2\pi ni/N} \quad \text{for } n = 0, ..., (N\text{-}1) \quad (15)$$

and Eq. (13) can be evaluated using the IFFT formula

$$A_s(t)e^{j\phi_s(t)} = A_0\left[\frac{1}{N}\sum_{n=0}^{N-1}\bar{f}(n,t)[1+\eta_n\mu(t)]e^{j\frac{1}{2}\eta_n^2/\psi(t)}e^{j\eta_n[x_{pv}(t)+\delta xN/2]}\right] \quad (16)$$

where the spatial grid of the FFT/IFFT extends from $-\delta xN/2$ to $+\delta x(N/2-1)$, where n is the spatial frequency index of the FFT/IFFT operations, and where the n^{th} spatial frequency is

$$\eta_n = \begin{cases} 2\pi n/(N\delta x) & \text{if } n \le N/2 \\ 2\pi(n-N)/(N\delta x) & \text{if } N/2 < n \end{cases} \quad (17)$$

Standard FFT/IFFT calculations do not need to make the distinction between the low-n and high-n frequency formulas of Eq. (17). Normally, η_n only appears in the final factor of Eq. (16) where, because of the usual aliasing effect, the difference between the two versions of η_n has no impact if $x_{pv}(t)$ is a multiple of δx. Contrary to standard IFFT notation, η_n appears explicitly wherever it is needed in Eq. (16) because the usual aliasing rules do not apply. The low-n and high-n distinctions in Eq. (17) are needed in order to enforce the spatial bandwidth limitation assumption about the function $\exp\{j\Delta\bar{\phi}(\Delta x)/\hat{k}_3(t)\}$.

The time t is a parameter in the calculations of Eqs. (15) and (16). Therefore, these equations need to be re-evaluated for each measurement sample time t_l. This need to re-calculate causes an inefficient use of the FFT and IFFT formulas in these equations. Suppose, on the other hand, that the quantities $\hat{k}_3$, μ, and ψ did not depend on t. Suppose, also, that the sample times t_l had been chosen to yield the relationship $x_{pv}(t_l) = (l\text{-}N/2)\delta x$. Then a single FFT operation in Eq. (15) and a single IFFT operation in Eq. (16) would suffice to determine the scintillation phasor $A_s(t_l)exp[j\phi_s(t_l)]$ for all sample times l = 0, ..., (N-1). Given the reality, however, the most efficient implementation of these operations uses a full FFT calculation in Eq. (15) at each sample time t_l, but it performs the IFFT operations in Eq. (16) only for the single spatial point $x_{pv}(t_l)$. That is, only a single brute-force summation of the form given in Eq. (16) is performed. The usual IFFT algorithm is not used to evaluate this sum because its operations are efficient only under the assumption that the sum needs to be performed for the N evenly spaced pierce-point values $x_{pv}(t_l) = (l\text{-}N/2)\delta x$ for l = 0, ..., (N-1).

Note that the spatial bandwidth limitation assumption of the FFT/IFFT calculations must be considered carefully. It is a limitation on the bandwidth $\exp\{j\Delta\bar{\phi}(\Delta x)/\hat{k}_3(t)\}$, which is not identical to a bandwidth limitation on $VTEC(\Delta x)$ because $\exp\{j\Delta\bar{\phi}(\Delta x)/\hat{k}_3(t)\}$ is a nonlinear function of $VTEC(\Delta x)$ even though $\Delta\bar{\phi}(\Delta x)$ is a linear function of $VTEC(\Delta x)$. The most obvious feature of this nonlinear dependence is that a large slope of $VTEC(\Delta x)$ vs. Δx can lead to a large spatial bandwidth of $\exp\{j\Delta\bar{\phi}(\Delta x)/\hat{k}_3(t)\}$ as a result of the cosine and sine functions that are involved in the calculation of a complex exponential. This means that a low-bandwidth function $VTEC(\Delta x)$ that has large values, and therefore large slopes, can lead to a high bandwidth $\exp\{j\Delta\bar{\phi}(\Delta x)/\hat{k}_3(t)\}$. Therefore, account must be taken of this nonlinear relationship when selecting the FFT sample interval δx.

The impact of the FFT periodicity assumption can be kept low by choosing a long enough periodicity interval $N\delta x$.

The Huygens-Fresnel integral in Eq. (9) can be thought of as a kind of spatial filter that acts on the phase changes that are caused by the $VTEC(x)$ distribution. The important filtering term is $exp\{-\frac{1}{2}\psi(t)\Delta x^2\}$. It has the effect of passing low frequency phase variations of $\exp\{j\Delta\bar{\phi}(\Delta x)/\hat{k}_3(t)\}$ that occur near the ionospheric pierce point of the LOS. Remote from the pierce point, it only allows influence from very high frequency $\exp\{j\Delta\bar{\phi}(\Delta x)/\hat{k}_3(t)\}$ variations. Given that the actual and modeled $\exp\{j\Delta\bar{\phi}(\Delta x)/\hat{k}_3(t)\}$ bandwidths are limited, these limitations translate into limitations on the spatial extent from the LOS pierce point of the $VTEC(x)$ values that affect the received signal. Suppose that one assumes typical values of ψ in the $exp\{-\frac{1}{2}\psi(t)\Delta x^2\}$ filtering term and that one analyzes the ability of this term to transmit the effects of various spatial frequencies at points that are more than 25 km removed from the pierce point. Such an analysis shows that the significant frequencies of $\exp\{j\Delta\bar{\phi}(\Delta x)/\hat{k}_3(t)\}$ are greater than 0.1 cycles/meter in this remote region. Spatial bandwidths in this range are unrealistic. Therefore, one can be confident that the un-physical FFT periodicity assumption will not degrade the model fidelity if the FFT window extends more than 25 km past either end of the possible $x_{pv}(t)$ pierce points.

E. Calculation of Ionospheric Group Delay using the Phase-Screen Model

The dual-frequency GPS receiver that has been used to collect data for this study is capable of measuring the differential group delay between the received L1 and L2 signals. Therefore, it was thought wise to develop a model of how the disturbed $VTEC(x)$ vs. x distribution affects group delay. One might be tempted to use the usual formula for a quiescent ionosphere as found in Ref. 15. This would work out to $\tau_{gd}(t,\omega) = \Delta\bar{\phi}[x_{pv}(t)]/[\omega\hat{k}_3(t)]$ because the pierce point relative to the convected $VTEC(x)$ vs. x distribution is $x_{pv}(t)$. Unfortunately, this formula does not account for the fact that $VTEC(x)$ values in the neighborhood of $x_{pv}(t)$ also affect the group delay. Therefore, a new formula is needed.

The needed formula for τ_{gd} has been derived by recognizing that $\tau_{gd} = -\partial\phi/\partial\omega$ for a dispersive medium, where ϕ is the carrier phase advance that is caused by the medium. In the case of the diffraction calculations of Eqs. (15) and (16), the group delay is $\tau_{gd}(t,\omega) = -\partial\phi_s/\partial\omega$ with ϕ_s being the phase of the phasor that is determined by Eq. (16).

The detailed computation of $\tau_{gd}(t,\omega)$ relies on differentiation of the formulas in Eqs. (15) and (16) with respect to ω. Suppose that the bracketed inverse Fourier sum on the right-hand side of Eq. (16) produces the result $a(t,\omega)+jb(t,\omega)$, where the functions $a(t,\omega)$ and $b(t,\omega)$ are real-valued. Then the group delay caused by the phase-screen model is

$$\tau_{gd}(t,\omega) = \frac{a(t,\omega)\left.\frac{\partial b}{\partial\omega}\right|_{(t,\omega)} - b(t,\omega)\left.\frac{\partial a}{\partial\omega}\right|_{(t,\omega)}}{a^2(t,\omega)+b^2(t,\omega)} \qquad (18)$$

Computation of the partial derivatives $\partial a/\partial\omega$ and $\partial b/\partial\omega$ starts with partial differentiation with respect to ω of the Fourier sum on the right-hand side of Eq. (15). It depends on ω because the function $\Delta\bar{\phi}(\Delta x)$ depends on ω, as per Eq. (1). This partial differentiation results in a sum that is the Fourier transform of a set of partial derivatives, and it can be evaluated very efficiently using FFT techniques. The partial derivative calculations are completed by differentiation with respect to ω of the inverse Fourier sum on the right-hand side of Eq. (16). It depends on ω because the functions $\bar{f}(n,t)$, $\mu(t)$, and $\psi(t)$ depend on ω, as per Eqs. (15), (12), and (10a). The resulting sum is the inverse Fourier transform of another set of partial derivatives. Derivation of the formulas for the partial derivative FFT and IFFT sums is straightforward. These derivations have been omitted for the sake of brevity.

III. NONLINEAR LEAST-SQUARES INVERSE DIFFRACTION CALCULATIONS

This section develops techniques to invert the phase-screen model of Eqs. (1)-(17) so that measurement of scintillating $A_s(t)exp\{j\phi_s(t)\}$ phasors can be used to infer the $VTEC(x)$ distribution that caused them. This technique is developed for use with dual-frequency data for the GPS L1 and L2 frequencies. The model inversion technique is based on standard nonlinear least-squares methods [17].

A. Dual-Frequency Accumulation Measurement Model

The GPS receiver measures in-phase and quadrature accumulations at the L1 and L2 frequencies. These accumulations are complex phasor representations of the received amplitude and phase. This section models these accumulations as functions of the ionosphere geometric parameters h and γ, the ionosphere west-to-east drift velocity v, the $VTEC(x)$ distribution, and miscellaneous "slop" parameters. These slop parameters are needed in order to account for unavoidable real-world effects on the data. These effects include multi-path, antenna gain pattern variations, and the residual phase effects of modeling errors in the range $\rho_{asc}(t)$, in the neutral

atmosphere delay $\tau_{na}(t)$, and in the receiver clock error. The nonlinear least-squares algorithm estimates both the additional unknown parameters that characterize each slop term and the original quantities of interest.

The primary effects of code multi-path and of antenna gain pattern variation are likely to be slow variations of the received amplitude of each signal. Such slow variations, as measured relative to the rapid amplitude variations that are caused by scintillation, have been observed in the recorded data. The slop parameters that model these effects are coefficients in time polynomials that characterize the resulting signal amplitude variations. These polynomials take the form:

$$\Delta G_{L1}(t) = g_{11}(t-t_0) + \tfrac{1}{2} g_{12}(t-t_0)^2 + \ldots + \tfrac{1}{M!} g_{1M}(t-t_0)^M \qquad (19a)$$

$$\Delta G_{L2}(t) = g_{21}(t-t_0) + \tfrac{1}{2} g_{22}(t-t_0)^2 + \ldots + \tfrac{1}{M!} g_{2M}(t-t_0)^M \qquad (19b)$$

where ΔG_{L1} and ΔG_{L2} are, respectively, the equivalent L1 and L2 gain perturbations in dB, g_{11}, ..., g_{1M} and g_{21}, ..., g_{2M} are the unknown coefficients in the respective ΔG_{L1} and ΔG_{L2} polynomials, and M is the order of each polynomial. The corresponding amplitude scale factors are $exp\{s\Delta G_{L1}(t)\}$ and $exp\{s\Delta G_{L2}(t)\}$ where $s = ln(10)/20$. If ΔG_{L1} or ΔG_{L2} equals 0 dB, then the corresponding amplitude scale factor equals 1.

The carrier phase slop factors include an initial carrier phase bias and the effects of residual $\rho_{asc}(t)$ and $\tau_{na}(t)$ modeling errors and receiver clock errors. The polynomial that models the last three phase effects is given in equivalent time units:

$$\Delta\tau_{\rho na}(t) = \Delta\tau_1(t-t_0) + \tfrac{1}{2}\Delta\tau_2(t-t_0)^2 + \ldots + \tfrac{1}{T!}\Delta\tau_T(t-t_0)^T \qquad (20)$$

where $\Delta\tau_{\rho na}$ is the equivalent delay error, $\Delta\tau_1$, ..., $\Delta\tau_T$ are the unknown delay model polynomial coefficients, and T is the order of the delay slop polynomial. The residual phase slop models at the two GPS carrier frequencies are then

$$\Delta\phi_{L1}(t) = \omega_{L1}\Delta\tau_{\rho na}(t) + \Delta\phi_{L10} \qquad (21a)$$

$$\Delta\phi_{L2}(t) = \omega_{L2}\Delta\tau_{\rho na}(t) + \Delta\phi_{L20} \qquad (21b)$$

$\omega_{L1} = 2\pi\times 1575.42\times 10^6$ rad/sec and $\omega_{L1} = 2\pi\times 1227.6\times 10^6$ rad/sec are, respectively, the nominal carrier frequencies of the GPS L1 and L2 signals. $\Delta\phi_{L10}$ and $\Delta\phi_{L20}$ are the associated initial carrier phase ambiguities.

The slop parameter models in Eqs. (19a)-(21b) along with the phase-screen model in Eqs. (1)-(17) can be combined in order to form the complete model of the dual-frequency in-phase and quadrature accumulations. This model takes the form:

$$I_{L1}(t) = A_{L10}e^{s\Delta G_{L1}(t)} \times \{a(t,\omega_{L1})cos[\Delta\phi_{L1}(t)] - b(t,\omega_{L1})sin[\Delta\phi_{L1}(t)]\} \qquad (22a)$$

$$Q_{L1}(t) = A_{L10}e^{s\Delta G_{L1}(t)} \times \{a(t,\omega_{L1})sin[\Delta\phi_{L1}(t)] + b(t,\omega_{L1})cos[\Delta\phi_{L1}(t)]\} \qquad (22b)$$

$$I_{L2}(t) = A_{L20}e^{s\Delta G_{L2}(t)} \times \{a(t,\omega_{L2})cos[\Delta\phi_{L2}(t)] - b(t,\omega_{L2})sin[\Delta\phi_{L2}(t)]\} \qquad (22c)$$

$$Q_{L2}(t) = A_{L20}e^{s\Delta G_{L2}(t)} \times \{a(t,\omega_{L2})sin[\Delta\phi_{L2}(t)] + b(t,\omega_{L2})cos[\Delta\phi_{L2}(t)]\} \qquad (22d)$$

where I_{L1} and I_{L2} are the in-phase accumulations for the L1 and L2 signals and Q_{L1} and Q_{L2} are the corresponding quadrature accumulations. The quantities A_{L10} and A_{L20} are the equivalent L1 and L2 accumulation amplitudes that would have been measured if there had been no scintillation and no antenna/multi-path gain variations.

Recall from the discussion of group delay in Section II that the quantities $a(t,\omega)$ and $b(t,\omega)$ are, respectively, the real and imaginary parts of the bracketed IFFT sum on the right-hand side of Eq. (16). As appropriate, they are evaluated at the frequency ω_{L1} in the L1 accumulation models and at the frequency ω_{L2} in the L2 accumulation models. Note that these two functions also depend on the vertical total electron density distribution $VTEC(x)$ vs. x and on the ionospheric altitude h, tilt γ, and drift velocity v. The dependence on h and γ comes through the influence of these two quantities on $\hat{k}_1(t)$, $\hat{k}_3(t)$, $\hat{k}_{10}$, $\hat{k}_{30}$, and z_a. The dependence on v comes through its affect on $x_{pv}(t)$.

B. Spline Model of *VTEC* Distribution

This effort's main goal is to estimate the vertical total electron content distribution $VTEC(x)$ vs. x. In principle, this is an infinite-dimensional estimation problem that is not tractable on a finite computer. Therefore, it is necessary to work with a finite-dimensional representation of $VTEC(x)$. The chosen representation is a cubic spline. The function $VTEC(x)$ is parameterized by its values and slopes at the spline node points.

The cubic spline formula for $VTEC(x)$ takes the form:

$$VTEC(x) = V_i\left\{1+\left(\frac{x-(x_{cmin}+i\delta x_c)}{\delta x_c}\right)^2\left[-3+2\left(\frac{x-(x_{cmin}+i\delta x_c)}{\delta x_c}\right)\right]\right\}$$

$$+V_{i+1}\left\{\left(\frac{x-(x_{cmin}+i\delta x_c)}{\delta x_c}\right)^2\left[3-2\left(\frac{x-(x_{cmin}+i\delta x_c)}{\delta x_c}\right)\right]\right\}$$
$$+V_i'\{x-(x_{cmin}+i\delta x_c)\}\times$$
$$\left\{1+\left(\frac{x-(x_{cmin}+i\delta x_c)}{\delta x_c}\right)\left[-2+\left(\frac{x-(x_{cmin}+i\delta x_c)}{\delta x_c}\right)\right]\right\}$$
$$+V_{i+1}'\{x-(x_{cmin}+i\delta x_c)\}\times$$
$$\left\{\left(\frac{x-(x_{cmin}+i\delta x_c)}{\delta x_c}\right)\left[-1+\left(\frac{x-(x_{cmin}+i\delta x_c)}{\delta x_c}\right)\right]\right\}$$
$$\text{for } x_{cmin}+i\delta x_c \le x < x_{cmin}+(i+1)\delta x_c \qquad (23)$$

This formula applies for the N_c spline intervals denoted by the index i; i can range from 0 to N_c-1. Each value of x in the range $x_{cmin} \le x < x_{cmin}+N_c\delta x_c$ lies in one of these intervals. This formula parameterizes $VTEC(x)$ using $2N_c$ parameters, the N_c+1 spline node values V_i for i = 0, ..., N_c and the N_c-1 spline node slopes V_i' for i = 1, ..., (N_c-1). The two end-point slopes are constrained to be zero, i.e., $V_0' = V_{N_c}' = 0$. The displacement x_{cmin} is the minimum range of the spline, and the increment δx_c is the length of each spline interval.

Normally the interval from x_{cmin} to $x_{cmax} = x_{cmin}+N_c\delta x_c$, which is the union of all of the spline intervals, is chosen to include all possible pierce point positions as measured relative to the drifting $VTEC(x)$ distribution. In other words, it is chosen so that $x_{cmin} < x_{pv}(t_l) < x_{cmax}$ for all sample times t_l for which accumulation data are available. In practice, x_{cmin} is normally chosen to be significantly lower than the minimum $x_{pv}(t_l)$ value, x_{pvmin}, and x_{cmax} is normally chosen to be significantly higher than the maximum $x_{pv}(t_l)$ value, x_{pvmax}.

As discussed in Section II, there is a need to extend the FFT summation in Eq. (15) well below x_{pvmin} and well above x_{pvmax} in order to avoid ill effects from the unphysical FFT periodicity assumption. In order to do this, it is necessary to extend the definition of $VTEC(x)$ below x_{cmin} and above x_{cmax} and to make it be periodic of period $N\delta x$. This is accomplished as follows: Periodicity is enforced by making a smooth, cubically-splined transition from the high-x value V_{N_c} that occurs at the end of one period to the low-x value V_0 that occurs at the beginning of the next period. The spline that accomplishes the periodicity transition starts at $x = 0.5N\delta x-\delta x_{per}$ in the high-x region and extends to $0.5N\delta x+\delta x_{per}$. An identical transition occurs in the range $-0.5N\delta x-\delta x_{per} \le x < -0.5N\delta x+\delta x_{per}$ in the low-x region. There are two additional regions to consider, buffer regions that lie between the periodicity transition regions and the regular spline region of Eq. (23). The low-x buffer region covers the range $-0.5N\delta x+\delta x_{per} \le x < x_{cmin}$. In this region, $VTEC(x)$ is constant and equals its value at the low end of the regular spline region: $VTEC(x) = V_0$. The high-x buffer region is $x_{cmax} \le x < 0.5N\delta x-\delta x_{per}$, and $VTEC(x) = V_{N_c}$ is the constant total electron content in this region. The formulas for $VTEC(x)$ in the periodicity transition regions are:

$$VTEC(x) =$$
$$V_{N_c}\left\{1+\left(\frac{x+(0.5N\delta x+\delta x_{per})}{2\delta x_{per}}\right)^2\left[-3+2\left(\frac{x+(0.5N\delta x+\delta x_{per})}{2\delta x_{per}}\right)\right]\right\}$$
$$+V_0\left\{\left(\frac{x+(0.5N\delta x+\delta x_{per})}{2\delta x_{per}}\right)^2\left[3-2\left(\frac{x+(0.5N\delta x+\delta x_{per})}{2\delta x_{per}}\right)\right]\right\}$$
$$\text{for } -0.5N\delta x-\delta x_{per} \le x < -0.5N\delta x+\delta x_{per} \qquad (24a)$$

$$VTEC(x) =$$
$$V_{N_c}\left\{1+\left(\frac{x-(0.5N\delta x-\delta x_{per})}{2\delta x_{per}}\right)^2\left[-3+2\left(\frac{x-(0.5N\delta x-\delta x_{per})}{2\delta x_{per}}\right)\right]\right\}$$
$$+V_0\left\{\left(\frac{x-(0.5N\delta x-\delta x_{per})}{2\delta x_{per}}\right)^2\left[3-2\left(\frac{x-(0.5N\delta x-\delta x_{per})}{2\delta x_{per}}\right)\right]\right\}$$
$$\text{for } 0.5N\delta x-\delta x_{per} \le x < 0.5N\delta x+\delta x_{per} \qquad (24b)$$

An example cubic-spline representation of $VTEC(x)$ is shown in Fig. 3. This distribution includes N_c = 14 spline intervals in its central cubic-spline region. This central region extends from x_{cmin} = -25 km to x_{cmax} = +25 km, and it uses a spline grid interval of δx_c = 3.571 km. The FFT periodicity interval is $N\delta x$ = 120 km, which extends out to ± 60 km, well past the ends of the central spline region. The half-width of the lower and upper periodicity-transition spline intervals is δx_{per} = 10 km. This spline is fully characterized by the 28 estimation parameters V_0, ..., V_{14} and V'_1, ..., V'_{13}.

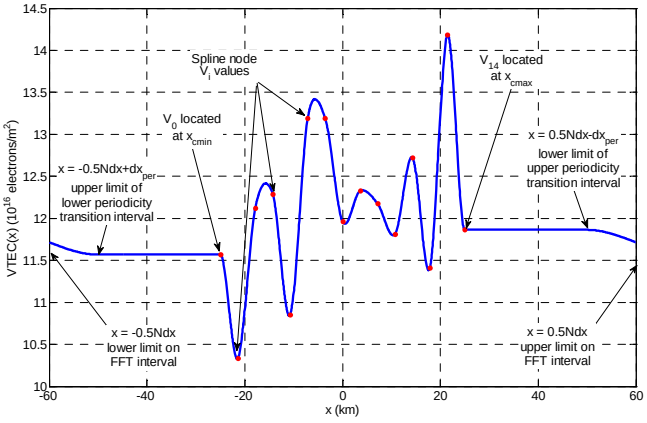

Fig. 3. An example cubic spline representation of a VTEC(x) vs. x distribution.

Useful $VTEC(x)$ splines typically have many more spline

nodes and a much finer spline grid spacing δx_c than are depicted in Fig. 3. The finer grid spacing is needed so that the spline will be able to capture the fine-scale electron density variations that cause scintillation.

Note that a reasonable approximation of the maximum spatial bandwidth of this spline is $1/\delta x_c$ cycles/m, i.e., one cycle per spline interval.

C. Estimated Unknowns

The nonlinear least-squares estimation problem and the associated solution algorithm can be discussed more easily if one groups the estimated quantities into a single vector of unknowns. This vector takes the form

$$\begin{aligned} X = [\, & V_0; V_1; V_2; ...; V_{N_c}; V_1'; V_2'; V_3'; ...; V_{N_c-1}'; \\ & h; \gamma; v; A_{L10}; A_{L20}; \Delta\phi_{L10}; \Delta\phi_{L20}; \Delta\tau_1; \Delta\tau_2; \\ & \Delta\tau_3; ...; \Delta\tau_T; g_{11}; g_{12}; g_{13}; ..., g_{1M}; g_{21}; g_{22}; \\ & g_{23}; ..., g_{2M}] \end{aligned} \tag{25}$$

It includes the function and slope values of $VTEC(x)$ at its cubic-spline nodes, the altitude and tilt of the ionospheric phase-screen plane, the west-to-east drift velocity of the "frozen" $VTEC(x)$ distribution, the nominal accumulation amplitudes at the two GPS frequencies, the carrier phase ambiguities at the two frequencies, the coefficients of the residual phase/timing slop polynomial, and that coefficients of the gain slop polynomials at the two frequencies. This vector has $N_X = 2N_c+7+T+2M$ elements.

D. *A Priori* Information/Soft Constraints

It was originally unclear whether the vector of unknowns in Eq. (25) would be observable based on the measurement model in Eqs. (22a) to (22d). Observability is the condition where only a unique value of the X vector of unknowns can satisfy all of the measurement equations. Although the measurement equations are non-linear, one can usually rely in intuition from linear equations and draw the immediate conclusion that the number of measurements must be greater than or equal to the number of unknowns in order for observability to hold. This implies that the number of independent measurement samples $[I_{L1}(t_l); Q_{L1}(t_l); I_{L2}(t_l); Q_{L2}(t_l)]$ for $l = 1, ..., L$ must obey the relationship $4L \geq N_X$.

Even given enough measurements, the vector of unknowns X may not be fully observable. There may be manifolds in X space (i.e., subsets that contain many points) that all produce identical dual-frequency accumulation measurements at all of the sample times. In this situation, one can add *a priori* information about the unknowns if such information is available. The hope is that this added information will cause the corresponding estimation problem to have a unique optimal solution. In some cases, *a priori* information can be derived directly from physical principles or from auxiliary data. In other cases, the *a priori* information may be somewhat ad hoc. In these latter cases, the resulting information acts as a "soft" penalty-type constraint on the solution. The *a priori* information that has been used in the present case is primarily of this latter type. The resulting ad hoc constraints have been made rather loose based on an *a priori* sense of what is "reasonable" for this problem.

The ad hoc *a priori* information takes the form of a set of penalty terms that get added to the squared-error cost function. These penalty terms are as follows:

The 3rd derivative of the $VTEC(x)$ cubic spline is penalized near its ends:

$$\Delta J_{V'''}(X) = \frac{1}{2\sigma_{V'''}^2} \sum_{i=0}^{N_c-1} w_i''' \left\{ \frac{12}{\delta x_c^3}[V_i - V_{i+1}] + \frac{6}{\delta x_c^2}[V_i' + V_{i+1}'] \right\}^2 \tag{26}$$

where $\sigma_{V'''}$ is the *a priori* standard deviation of the weighted root mean square of the 3rd derivatives in the end regions where the w_i''' weightings are non-zero. This weighting factor varies with the spline interval index as follows:

$$w_i''' = \begin{cases} \dfrac{1}{2N_{w23}+\Delta N_{w23}} & i \leq N_{w23}-1 \\ \dfrac{(N_{w23}+\Delta N_{w23}-1)-i}{\Delta N_{w23}(2N_{w23}+\Delta N_{w23})} & N_{w23}-1 < i \leq N_{w23}+\Delta N_{w23}-1 \\ 0 & N_{w23}+\Delta N_{w23}-1 < i < N_c-N_{w23}-\Delta N_{w23} \\ \dfrac{i-(N_c-N_{w23}-\Delta N_{w23})}{\Delta N_{w23}(2N_{w23}+\Delta N_{w23})} & N_c-N_{w23}-\Delta N_{w23} \leq i < N_c-N_{w23} \\ \dfrac{1}{2N_{w23}+\Delta N_{w23}} & N_c-N_{w23} \leq i \end{cases} \tag{27}$$

this weighting scheme applies full weight to the squares of the 3rd derivatives in the N_{w23} spline intervals at each end of the $VTEC(x)$ central cubic spline region, and the weighting decays linearly to zero in the ΔN_{w23} spline intervals that lie just inside these outer intervals of full weight. The idea is to select N_{w23} and ΔN_{w23} to be relatively small compared to the total number of spline intervals N_c and to make the penalized intervals lie outside the region of actual pierce points, i.e., outside the data interval $x_{pvmin} < x < x_{pvmax}$. These penalty terms are deemed necessary at spline intervals that lie significantly outside of this interval because there is a decaying effect of the corresponding $VTEC(x)$ values on the modeled accumulations in Eqs. (22a)-(22d). This reduced influence in the measurement models causes the function and slope values at the outer spline grid points to be nearly unobservable. The addition of this penalty term ameliorates this problematic tendency.

A second set of penalties that serve a similar purpose are placed on the discontinuities of the $VTEC(x)$ 2nd derivatives that can occur at spline node points outside of the data interval $x_{pvmin} < x < x_{pvmax}$. The sum of these terms takes the form:

$$\Delta J_{\Delta V''}(X) = \frac{1}{2\sigma_{\Delta V''}^2} \sum_{i=1}^{N_c-1} w_i'' \times \left\{ \frac{6}{\delta x_c^2}[-V_{i-1} + V_{i+1}] - \frac{2}{\delta x_c}[V'_{i-1} + 4V'_i + V'_{i+1}] \right\}^2 \quad (28)$$

where $\sigma_{\Delta V''}$ is the *a priori* standard deviation of the weighted root mean square of the 2nd derivative discontinuities in the end regions. The weighting factor w_i'' varies with the spline node index as follows:

$$w_i'' = \begin{cases} \dfrac{1}{2N_{w23} + \Delta N_{w23}} & i \le N_{w23} \\ \dfrac{(N_{w23} + \Delta N_{w23}) - i}{\Delta N_{w23}(2N_{w23} + \Delta N_{w23})} & N_{w23} < i \le N_{w23} + \Delta N_{w23} \\ 0 & N_{w23} + \Delta N_{w23} < i < N_c - N_{w23} - \Delta N_{w23} \\ \dfrac{i - (N_c - N_{w23} - \Delta N_{w23})}{\Delta N_{w23}(2N_{w23} + \Delta N_{w23})} & N_c - N_{w23} - \Delta N_{w23} \le i < N_c - N_{w23} \\ \dfrac{1}{2N_{w23} + \Delta N_{w23}} & N_c - N_{w23} \le i \end{cases} \quad (29)$$

which is similar to the variation of the w_i''' weighting factor, except that w_i'' is defined over a set of spline indices that has one less element.

The third *a priori* weighting term penalizes non-zero values of the time-equivalent common-mode phase slop from Eq. (20). This penalty term takes the form

$$\Delta J_{\Delta\tau}(X) = \frac{1}{2L\sigma_{\Delta\tau}^2} \sum_{l=1}^{L} [\Delta\tau_{\rho na}(t_l)]^2 \quad (30)$$

where $\sigma_{\Delta\tau}$ is the *a priori* standard deviation of the root mean square of the time-equivalent common-mode slop as averaged over the data sample times.

The fourth *a priori* weighting term penalizes non-zero time derivatives of the antenna-gain/multi-path slop functions for the two frequencies. Recall that these functions have been defined in Eqs. (19a)-(19b). This penalty term is

$$\Delta J_{\Delta G}(X) = \frac{1}{2\sigma_{\Delta G'}^2} \left\{ \frac{1}{L} \sum_{l=1}^{L} \left[\left. \frac{d\Delta G_{L1}}{dt} \right|_{t_l} \right]^2 + \frac{1}{L} \sum_{l=1}^{L} \left[\left. \frac{d\Delta G_{L2}}{dt} \right|_{t_l} \right]^2 \right\} \quad (31)$$

where $\sigma_{\Delta G'}$ is the *a priori* standard deviation of the root mean square of the time derivative of each gain slop factor averaged over the data samples.

The remaining *a priori* penalty terms can be lumped together to form

$$\Delta J_{\overline{V}h\gamma v}(X) = \frac{1}{2\sigma_{\overline{V}}^2} \left[\overline{V}_{nom} - \frac{1}{N_c} \sum_{i=0}^{N_c} V_i \right]^2 + \frac{1}{2\sigma_h^2}[h_{nom} - h]^2 + \frac{1}{2\sigma_\gamma^2}[\gamma_{nom} - \gamma]^2 + \frac{1}{2\sigma_v^2}[v_{nom} - v]^2 \quad (32)$$

where $\overline{V}_{nom}$, h_{nom}, γ_{nom}, and v_{nom} are the *a priori* estimates of, respectively, the mean of $VTEC(x)$ at the spline node points and the ionosphere's altitude, tilt angle, and drift velocity. The corresponding *a priori* standard deviations are $\sigma_{\overline{V}}$, σ_h, σ_γ, and σ_v.

Of all of the *a priori* penalty terms, the first one in Eq. (32), the $\overline{V}_{nom}$ term, is the only one that is known definitely to be needed in order to make the estimation problem observable. Without this term, the mean *VTEC* mean value $\overline{V}$ and the phase ambiguities $\Delta\phi_{L10}$ and $\Delta\phi_{L20}$ can vary together in a way that leaves all of the accumulations in Eqs. (22a)-(22d) unaffected for all sample times. This fact seems obvious in hindsight, but it was not discovered until after initial attempts had been made to perform estimation without this term.

All of the *a priori* standard deviations that are used in Eqs. (26), (28), and (30)-(32) are set to relatively large values. This strategy biases the nonlinear estimation algorithm toward letting the accumulation data determine the values of all observable elements of X. It relegates the *a priori* penalty terms to two roles. One role is to keep any unobservable or nearly unobservable modes in X space from taking on ridiculous values. The other role is to keep the optimal estimation search directions from taking on unreasonable values that would tend to retard the progress of the nonlinear least-squares solution algorithm.

E. Least-Squares Cost Function and Minimization using Gauss-Newton and Levenberg-Marquardt Algorithms

Estimation of the vector of unknowns X is accomplished by batch minimization of a squared-error cost function. The following cost function is minimized:

$$\begin{aligned} J(X) = {} & \frac{1}{2\sigma_{IQL1}^2} \sum_{l=1}^{L} [I_{L1meas}(t_l) - I_{L1model}(t_l;X)]^2 \\ & + \frac{1}{2\sigma_{IQL1}^2} \sum_{l=1}^{L} [Q_{L1meas}(t_l) - Q_{L1model}(t_l;X)]^2 \\ & + \frac{1}{2\sigma_{IQL2}^2} \sum_{l=1}^{L} [I_{L2meas}(t_l) - I_{L2model}(t_l;X)]^2 \\ & + \frac{1}{2\sigma_{IQL2}^2} \sum_{l=1}^{L} [Q_{L2meas}(t_l) - Q_{L2model}(t_l;X)]^2 \\ & + \Delta J_{V'''}(X) + \Delta J_{\Delta V''}(X) + \Delta J_{\Delta\tau}(X) \end{aligned}$$

$$+\Delta J_{\Delta G}(X) + \Delta J_{\overline{V}h\gamma\nu}(X) \qquad (33)$$

σ_{IQL1} and σ_{IQL2} are the standard deviations of the measurement errors in the measured in-phase and quadrature accumulations at the L1 and L2 frequencies. The corresponding measured accumulations are $I_{L1meas}(t_l)$, $Q_{L1meas}(t_l)$, $I_{L2meas}(t_l)$, and $Q_{L2meas}(t_l)$. The associated modeled values of these accumulations, $I_{L1model}(t_l;X)$, $Q_{L1model}(t_l;X)$, $I_{L2model}(t_l;X)$, and $Q_{L2model}(t_l;X)$, are computed as functions of the elements of X by using the phase-screen model equations of Section II. They are equal to the right-hand-side expressions in Eqs. (22a)-(22d).

Note that the squared-error cost function in Eq. (33) does not include the ionospheric group delay at either frequency. That is, it does not include terms involving either $\tau_{gd}(t,\omega_{L1})$ or $\tau_{gd}(t,\omega_{L2})$ as modeled by Eq. (18). Measurements of these quantities have been omitted because consideration of the actual receiver data indicated that the quality of the group delay data was poor. The estimation problem would need to estimate an L1/L2 differential line bias, which would mean that only high-frequency variations of the group delay would affect the $VTEC(x)$ estimate. These high-frequency estimates would have little impact due to the relatively high noise level in the associated group delay measurements. Given that the inclusion of $\tau_{gd}(t,\omega_{L1})$ and $\tau_{gd}(t,\omega_{L2})$ doubles the computational burden of solving the nonlinear estimation problem, the added burden was not deemed to be worthwhile and the group delay data have been omitted. Section II documents the group delay model primarily to serve as a guide to any future efforts that may have access to better quality group delay measurements.

If one recognizes that the *a priori* penalty terms in Eq. (33) can be expressed as a sum of squared residuals, then one can re-cast the squared-error cost function in the standard form:

$$J(X) = \frac{1}{2}\left[\boldsymbol{y} - \boldsymbol{h}(X)\right]^{\mathrm{T}}\left[\boldsymbol{y} - \boldsymbol{h}(X)\right] \qquad (34)$$

where $\boldsymbol{y}$ is a normalized measurement vector and where the vector function $\boldsymbol{h}(X)$ constitutes the nonlinear measurement model. This formulation treats *a priori* data as though they constitute measurements. The elements of $\boldsymbol{y}$ are $[I_{L1meas}(t_1)/\sigma_{IQL1}$, $Q_{L1meas}(t_1)/\sigma_{IQL1}$, $I_{L2meas}(t_1)/\sigma_{IQL2}$, $Q_{L2meas}(t_1)/\sigma_{IQL2}$, $I_{L1meas}(t_2)/\sigma_{IQL1}$, $Q_{L1meas}(t_2)/\sigma_{IQL1}$,...], and the elements of $\boldsymbol{h}(X)$ are $[I_{L1model}(t_1;X)/\sigma_{IQL1}$, $Q_{L1model}(t_1;X)/\sigma_{IQL1}$, $I_{L2model}(t_1;X)/\sigma_{IQL2}$, $Q_{L2model}(t_1;X)/\sigma_{IQL2}$, $I_{L1model}(t_2;X)/\sigma_{IQL1}$, $Q_{L1model}(t_2;X)/\sigma_{IQL1}$, ...].

The optimal estimate of the X vector is the value that minimizes the cost function given in Eq. (34). Standard methods exist to perform a gradient-based iterative search for this minimum. One is the Gauss-Newton method, and another is the Levenberg-Marquardt method [17]. Both of these methods start with a guess, call it X_g, and linearize the problem model about this guess in order to calculate an improved guess. The squared-error cost function associated with the linearized problem takes the form

$$\Delta J(\Delta X) = \frac{1}{2}\left[\Delta\boldsymbol{y} - H\Delta X\right]^{\mathrm{T}}\left[\Delta\boldsymbol{y} - H\Delta X\right] - \frac{1}{2}\Delta\boldsymbol{y}^{\mathrm{T}}\Delta\boldsymbol{y} \qquad (35)$$

where $\Delta X = X - X_g$, $\Delta\boldsymbol{y} = \boldsymbol{y} - \boldsymbol{h}(X_g)$, and $H = \partial\boldsymbol{h}/\partial X$.

The Gauss-Newton method solves for the optimal ΔX increment that minimizes the cost in Eq. (35). It is $\Delta X = (H^{\mathrm{T}}H)^{-1}H^{\mathrm{T}}\Delta\boldsymbol{y}$. The standard Levenberg-Marquardt method adds a penalty term of the form $(0.5/\alpha)\Delta X^{\mathrm{T}}\Delta X$ to the cost in Eq. (35) before computing the optimal ΔX increment. The positive parameter α effectively determines the step size of the increment. A small α value yields a very small increment that tends towards the steepest descent direction and that is guaranteed to produce a cost decrease, though it may not be much of a decrease. A large α value allows ΔX to approach the Gauss-Newton increment. It is very useful to be able to control the step size in this fashion in order to guarantee that the algorithm will converge at least to a local minimum of the cost function.

For the present estimation problem, it is helpful to use a modified form of the Levenberg-Marquardt penalty term. This term takes the form $(0.5/\alpha)\Delta X^{\mathrm{T}}D\Delta X$. The diagonal positive definite matrix D is formed by taking the matrix $H^{\mathrm{T}}H$ and setting all of its off-diagonal elements to zero. The resulting solution increment is $\Delta X = \alpha(D + \alpha H^{\mathrm{T}}H)^{-1}H^{\mathrm{T}}\Delta\boldsymbol{y}$. Note that the matrix inversions needed in order to compute ΔX in the Gauss-Newton and Levenberg-Marquardt methods can be implemented using matrix square-root techniques and the stable orthogonal/upper-triangular (QR) factorization [17].

The nonlinear least-squares algorithm executes a rudimentary line search in order to determine its step-size parameter α. It starts by trying $\alpha = \infty$, that is, by trying the Gauss-Newton ΔX increment. If that step produces a cost such that $J(X_g+\Delta X) - J(X_g)$ is negative not too much greater than the predicted cost decrement $\Delta J(\Delta X)$ from Eq. (35), then the Gauss-Newton increment is used to compute $X_{gnew} = X_g+\Delta X$, and the algorithm repeats itself starting from the new guess X_{gnew}.

If $J(X_g+\Delta X) - J(X_g)$ is not small enough, then the line search algorithm tries $\alpha = 1$ in its modified Levenberg-Marquardt method and calculates a new ΔX increment. At this point, it is helpful to think of ΔX as being a function of α, $\Delta X(\alpha)$. Next, the line search algorithm constructs a quadratic model of the cost variations with α that is based on the known values at $\alpha = 0$, $J(X_g)$, and at $\alpha = 1$, $J[X_g+\Delta X(1)]$, and on the known derivative of J with respect to α evaluated at $\alpha = 0$, $\mathrm{d}J/\mathrm{d}\alpha|_0 = -\Delta\boldsymbol{y}^{\mathrm{T}}HD^{-1}H^{\mathrm{T}}\Delta\boldsymbol{y}$. This quadratic cost increment model is used to make a new prediction of the optimal step-length parameter α if the quadratic model's second derivative is positive. This

involves scalar optimization of a quadratic in α. The new $J[X_g+\Delta X(\alpha)]$ value at the new α guess is used to refine the quadratic model and produce further changes in the proposed α until a reasonable decrease of $J[X_g+\Delta X(\alpha)]$ below $J(X_g)$ is achieved. If the initial quadratic model of J vs. α has a negative second derivative after the search-step and cost-function evaluation at $\alpha = 1$, then $J[X_g+\Delta X(1)] < J(X_g)$. This step is acceptable, but an ad hoc method is used in an attempt to find a larger α value that produces a lower value of the resulting $J[X_g+\Delta X(\alpha)]$. Regardless of the sign of the second derivative of the initial quadratic model of J vs. α, the final solution increment $\Delta X(\alpha)$ yields a reasonable cost decrease. The Levenberg-Marquardt step finishes by computing $X_{gnew} = X_g+\Delta X(\alpha)$ in order to prepare for another iteration.

The major iterations are terminated and the problem is declared "solved" after appropriate termination conditions have been satisfied. These conditions involve checks of whether ΔX is small, checks of whether $|\Delta J(\Delta X)|$ is small, and checks of whether α is large, i.e., whether the algorithm uses a ΔX increment that is nearly equal to the Gauss-Newton step.

F. FFT-Based Computation of Problem Jacobian

The problem model Jacobian $H = \partial \mathbf{h}/\partial X$ includes derivatives of the measurement model functions on the right-hand sides of Eqs. (22a)-(22d). The measurement model functions, in turn, are defined using the bracketed expression on the right-hand side of Eq. (16). The real part of this expression is defined to be $a(t,\omega)$, and its imaginary part is defined to be $jb(t,\omega)$; thus, the entire bracketed term in Eq. (16) equals $a(t,\omega)+jb(t,\omega)$. It would actually be more informative to write these two functions as $a(t,\omega;X)$ and $b(t,\omega;X)$ because they also depend on the following elements of X: V_0, ..., V_{N_c}, V_1', ..., V_{N_c-1}', h, γ, and v.

The computation of $\partial \mathbf{h}/\partial X$ involves computation of the derivatives of $a(t,\omega;X)$ and $b(t,\omega;X)$ with respect to the aforementioned elements of X. The required partial derivatives of $a(t,\omega;X)$ and $b(t,\omega;X)$ can be determined by differentiating Eqs. (15) and (16) with respect to each element of X, applying the chain rule for differentiation wherever appropriate. The dependence of $a(t,\omega;X)$ and $b(t,\omega;X)$ on the elements V_0, ..., V_{N_c}, V_1', ..., V_{N_c-1}' enters through the function $\Delta\bar{\phi}(x)$ in Eq. (15) because this phase increment function is proportional to $VTEC(x)$. The dependence on h and γ enters through the quantities $\hat{k}_3(t)$, $\mu(t)$, $\psi(t)$, and $x_{pv}(t)$, with the last 3 of these quantities depending on h and γ because they depend on one or more of the quantities $\hat{k}_1(t)$, $\hat{k}_3(t)$, $\hat{k}_{10}$, $\hat{k}_{30}$, and z_a. The dependence on v enters through $x_{pv}(t)$.

Differentiation of the FFT summation in Eq. (15) and of the IFFT summation in Eq. (16) with respect to an element of X results in a new pair of FFT and IFFT operations. The derivative calculations can be carried out by using an FFT operation for the derivative of Eq. (15) because each derivative of Eq. (15) retains the FFT form. One should use the brute-force sum that results from differentiation of Eq. (16) instead of an IFFT operation because the result is needed only at one $x_{pv}(t_l)$ value. When differentiating with respect to a spline node value V_m or with respect to a spline node derivative value V_m', it will normally be efficient to evaluate the differentiated summation in Eq. (15) using brute-force techniques rather than FFT techniques. This is true because the derivative of $exp\{j\Delta\bar{\phi}([i - N/2]\delta x)/\hat{k}_3(t)\}$ with respect to V_m or V_m' will be zero for all but a few values of the FFT grid sample index i. This is the case for all spline nodes except $m = 0$ and $m = N_c$. V_0 and V_{N_c} affect many FFT sample points because of the method by which the definition of $VTEC(x)$ has been extended past the spline limits x_{cmin} and x_{cmax}. Recall that this extension is discussed after Eq. (23) and in connection with Fig. 3.

G. Computed Estimation Error Covariance

The nonlinear least-squares estimation equations can be used to compute a covariance matrix for the error in the optimal estimate of X. Suppose that one uses the linearized measurement model implied by the cost function approximation of Eq. (35), $\Delta\mathbf{y} = H\Delta\mathbf{x}$. Suppose that the only sources of error in the estimate are the errors in the measurement equations and the errors between the various *a priori* values and their true values. Suppose, also, that these errors are zero-mean, Gaussian, and uncorrelated and that they have the standard deviations $\sigma_{V'''}$ in Eq. (26), $\sigma_{\Delta V''}$ in Eq. (28), $\sigma_{\Delta\tau}$ in Eq. (30), $\sigma_{\Delta G}$ in Eq. (31), $\sigma_{\bar{V}}$, σ_h, σ_γ, and σ_v in Eq. (32), and σ_{IQL1} and σ_{IQL2} in Eq. (33). Then the linearized estimation error covariance of the optimal X estimate will be [18]

$$P_{XX} = [H^{\mathrm{T}} H]^{-1} \tag{36}$$

with the Jacobian matrix H evaluated at the optimal X estimate. P_{XX} can be calculated in a numerically stable manner by using a QR factorization [17] of H and a matrix square-root computation.

H. Generation of the First Guess

The nonlinear least-squares iterative minimization algorithm must be started with a first guess of the solution, X_{g0}. It is important to use a fairly good first guess for two reasons. First, a poor first guess can cause the algorithm to converge to a local minimum of the squared-error cost function that is not the global

minimum and, therefore, not optimal. Such a sub-optimal solution could be a very poor estimate of the scintillation conditions. Second, even if the algorithm eventually converges to the global minimum, a better first guess can reduce the number of iterations required for convergence, thereby reducing the computation time. Given that typical execution times for this paper's algorithm are on the order of 4 hours per Gauss-Newton or Levenberg-Marquardt iteration, the importance of saving iterations is obvious.

The first-guess procedure that has been used for this analysis starts by guessing reasonable values for the altitude, the tilt angle, and the west-to-east drift rate of the ionospheric phase screen. These lie in the ranges 300 km $\le h \le$ 400 km, $-5^o \le \gamma \le 5^o$, and 100 m/sec $\le v \le$ 200 m/sec. These h and v ranges are roughly consistent with observations and analysis reported in Refs. 13 and 14. This γ range is purely an educated guess.

The first-guess procedure uses the measured carrier phases at the GPS L1 and L2 frequencies in order to develop a guess of the *TEC* value based on the usual ionospheric carrier phase advance model for a uniform ionosphere [15]. This *TEC* estimate is

$$TEC(t_l) = \frac{c\omega_{L1}\omega_{L2}}{(2\pi)^2\, 40.3(\omega_{L1}^2 - \omega_{L2}^2)} \times \{\omega_{L1}\phi_{L2meas}(t_l) - \omega_{L2}\phi_{L1meas}(t_l)\} + \overline{\Delta TEC} \quad (37)$$

where $\phi_{L1meas}(t_l) = atan2[Q_{L1meas}(t_l), I_{L1meas}(t_l)] + 2\pi n_{L1l}$ and $\phi_{L2meas}(t_l) = atan2[Q_{L2meas}(t_l), I_{L2meas}(t_l)] + 2\pi n_{L2l}$. In these expressions, *atan2*[,] is the usual 2-argument arctangent function, n_{L1l} is an integer cycle ambiguity that unwraps the 2π ambiguity of the *atan2* function in a way that makes $\phi_{L1meas}(t_{l-1})$ and $\phi_{L1meas}(t_l)$ differ by no more than $\pm\ \pi$ radians, and n_{L2l} is an integer cycle ambiguity that serves a similar unwrapping purpose for $\phi_{L2meas}(t_l)$. The constant $\Delta\overline{TEC}$ in Eq. (37) is chosen to cause the mean of $TEC(t_l)$ for l = 1,..., L to equal the mean that is predicted by the standard GPS Klobuchar model [15] for the given LOS path.

Each *TEC* value is multiplied by the inverse slant factor in order to form the *VTEC* estimate

$$VTEC[x_{pv}(t_l)] = TEC(t_l)\hat{k}_3(t_l) \quad \text{for } l = 1, 2, 3, \ldots, L \quad (38)$$

These initial estimates apply at the x locations $x_{pv}(t_1)$, $x_{pv}(t_2)$, $x_{pv}(t_3)$, ..., $x_{pv}(t_L)$. These estimates are then linearly interpolated onto the subset of the FFT grid points $(-0.5N)\delta x$, $(-0.5N+1)\delta x$, $(-0.5N+2)\delta x$, ..., $(0.5N-1)\delta x$ that lie between the minimum and maximum values of the time-sampled pierce points $x_{pv}(t_1)$, $x_{pv}(t_2)$, $x_{pv}(t_3)$, ..., $x_{pv}(t_L)$. At the remaining FFT grid points, the $VTEC(x)$ function is extended as a constant value, as in Fig. 3, except that a straight-line fit is made between the high-x and low-x constants in order to force this $VTEC(x)$ estimate to be periodic with period $N\delta x$. Thus, the periodicity preserving cubic sections of at either end of Fig. 3 are replaced by straight-line sections. The first-guess procedure next uses FFT techniques in order to filter the resulting $VTEC(x)$ vs. x. function in a way that eliminates all frequencies above the sampling frequency of the cubic spline, all frequencies above $1/\delta x_c$ cycles/meter. This process takes the FFT of the $VTEC(x)$ points, it applies a filter that zeros the FFT outputs associated with all frequencies whose magnitudes exceed $1/\delta x_c$ while leaving all other FFT outputs unchanged, and it takes the IFFT of the result. It yields the distribution $VTEC_{bl}(x)$ vs. x, The subscript $()_{bl}$ stands for "band limited." This distribution is linearly interpolated onto the spline grid points x_{cmin}, $x_{cmin}+\delta x_c$, $x_{cmin}+2\delta x_c$, ..., $x_{cmin}+N_c\delta x_c$ in order to produce the first guesses of the spline node values V_0, V_1, V_2, ..., V_{N_c}. The same process is modified in order to produce the first guesses of the spline node derivative values V_1', V_2', V_3', ..., V_{N_c-1}'. This modification involves multiplication of the FFT of the $VTEC_{bl}(x)$ vs. x distribution by the corresponding spatial frequencies before application of the IFFT. The result is $[dVTEC(x)/dx]_{bl}$ vs. x, and this result gets linearly interpolated in order to yield the V_i' first guesses.

A linear least-squares fit of the residual phases is used in order to generate first guesses of the phase ambiguities $\Delta\phi_{L10}$ and $\Delta\phi_{L20}$ and of the phase slop polynomial coefficients $\Delta\tau_1$, $\Delta\tau_2$, $\Delta\tau_3$, ..., $\Delta\tau_T$. The following phase model equations are solved in a least-squares sense in order to determine these first guesses:

$$\phi_{L1meas}(t_l) - \frac{(2\pi)^2\, 40.3TEC(t_l)}{c\omega_{L1}} = \Delta\phi_{L10} + \omega_{L1}[\Delta\tau_1(t-t_0) + \tfrac{1}{2}\Delta\tau_2(t-t_0)^2 + \ldots + \tfrac{1}{T!}\Delta\tau_T(t-t_0)^T] \quad \text{for } l = 1, \ldots, L \quad (39a)$$

$$\phi_{L2meas}(t_l) - \frac{(2\pi)^2\, 40.3TEC(t_l)}{c\omega_{L2}} = \Delta\phi_{L20} + \omega_{L2}[\Delta\tau_1(t-t_0) + \tfrac{1}{2}\Delta\tau_2(t-t_0)^2 + \ldots + \tfrac{1}{T!}\Delta\tau_T(t-t_0)^T] \quad \text{for } l = 1, \ldots, L \quad (39b)$$

Solution of this over-determined system of linear equations is carried out using standard QR-factorization-based methods [17].

The first guess of the amplitude A_{L10} is computed by

solving the following systems of $2L$ linear equations in 1 unknown:

$$I_{L1meas}(t_l) = A_{L10} cos[\phi_{L1\mathrm{mod}}(t_l)] \quad \text{for } l = 1, ..., L \tag{40a}$$

$$Q_{L1meas}(t_l) = A_{L10} sin[\phi_{L1\mathrm{mod}}(t_l)] \quad \text{for } l = 1, ..., L \tag{40a}$$

with

$$\phi_{L1\mathrm{mod}}(t_l) = \frac{(2\pi)^2 40.3 TEC(t_l)}{c\omega_{L1}} + \Delta\phi_{L10} + \omega_{L1}[\Delta\tau_1(t-t_0) + \tfrac{1}{2}\Delta\tau_2(t-t_0)^2 + \ldots + \tfrac{1}{T!}\Delta\tau_T(t-t_0)^T] \quad \text{for } l = 1, ..., L \tag{41}$$

where the values of $\Delta\phi_{L10}$ and of $\Delta\tau_1$, $\Delta\tau_2$, $\Delta\tau_3$, ..., $\Delta\tau_T$ in this definition are the first-guess values that have been derived by solving the least-squares problem in Eqs. (39a) and (39b). A similar method is used to determine the first guess of A_{L20} with the only difference being the substitution of L2 data and estimates for L1 data and estimates in Eqs. (40a)-(41).

The first guesses of the gain perturbation polynomial coefficients are set to zero. That is, the first guesses of the polynomial coefficients in Eqs. (19a) and (19b) are $g_{11} = g_{12} = g_{13} = ... = g_{1M} = g_{21} = g_{22} = g_{23} = ... = g_{2M} = 0$. These guesses complete the definition of the first guess of the entire X vector.

IV. COLLECTION AND PRE-PROCESSING OF DUAL-FREQUENCY SCINTILLATION DATA

Scintillation data have been collected and used to generate the $I_{L1meas}(t_l)$, $Q_{L1meas}(t_l)$, $I_{L2meas}(t_l)$, and $Q_{L2meas}(t_l)$ accumulation "measurements" that constitute the principal inputs to this paper's inverse diffraction algorithm. The raw data were collected in Jan. 2007 in Cachoeira Paulista, Brazil. They were recorded using a dual-frequency wide-band digital storage receiver. Afterwards, a MATLAB software receiver was used in an off-line mode to acquire and track the C/A code on the L1 frequency and the new civilian L2C CL code on the L2 frequency. These data and the methods used to process them are described in Ref. 10, especially in Section IV of that work.

A batch of the Ref. 10 data has been used to test the present inverse diffraction algorithm. It was recorded on 17 Jan. 2007 starting at about 00:15 UT. Its duration is 10 minutes. The signal from PRN 12, which as a Block IIR-M satellite that broadcasts the new L2C signals, experienced scintillation during this data interval. Its L1 S_4 index ranged as high as 0.4 during the batch, and its L2 S_4 index reached a peak value of 0.5.

The MATLAB software receiver methods of Ref. 10 have been used to acquire and track the L1 and L2 civilian signals of PRN 12, and 100 Hz I and Q accumulations have been computed for both frequencies. After having been derived using fairly standard reception techniques, these accumulations have been rotated in the [I;Q] plane in order to remove the effects of satellite motion, neutral atmosphere delay, transmitter clock error, receiver clock error, and phase-lock loop tracking error. The satellite motion effects and the transmitter clock error effects have been removed by using the known antenna location in conjunction with the broadcast ephemeris and clock corrections for PRN 12 for the period in question. The neutral atmosphere delay has been removed by using the Hopfield model as described in Ref. 19.

The receiver clock error has been removed by using signals from a satellite with minimal scintillation, PRN 26. This satellite's signals had all other errors than receiver clock errors removed from its phase outputs by using the receiver position along with satellite ephemeris and clock information and models of the ionosphere and neutral atmosphere. The remaining phase variations were assumed to be the result of receiver clock error. These variations were fit to a straight line, and the resulting straight line has been used as the receiver clock error model. Note that it contains a bias that does not affect anything other than the slop factors $\Delta\phi_{L10}$ and $\Delta\phi_{L20}$ in the estimator of Section III.

The resulting rotated, dual-frequency, 100-Hz I and Q accumulations for PRN 12 could be used directly in the Eq. (33) cost function, but down-sampled versions have been used instead. The required computation time per major Gauss-Newton or Levenberg-Marquardt iteration is proportional to the number of measurement samples L. Therefore, it is beneficial in terms of computation time to increase the sample interval $\Delta t = t_{l+1} - t_l$ as much as possible without losing information. Review of the 100 Hz $I_{L1meas}(t)$, $Q_{L1meas}(t)$, $I_{L2meas}(t)$, and $Q_{L2meas}(t)$ time histories revealed that a 1 Hz sampling rate would suffice to capture all of the dynamic amplitude and phase variations that had been caused by the scintillation [*].

The down-sampling from 100 Hz accumulations to 1 Hz accumulations has been carried out using a data fitting scheme. For a given accumulation type, I or Q on L1 or L2, this scheme fits all of the accumulations within 0.5 seconds of a desired interpolated sample time using a quadratic polynomial. It then uses that value of that polynomial at the target sample time as its interpolated accumulation. This procedure has the beneficial effect of averaging the 100 Hz accumulations as well as interpolating them in a way that produces very little

[*] The ability to capture the full scintillation dynamics using a 1 Hz sampling rate indicates that this weak scintillation had relatively slow time variations according to criteria defined in Ref. 4.

distortion of the signals' scintillation characteristics. The beneficial averaging process reduces the measurement error standard deviations in the 1 Hz accumulations by a factor of 6.67 from the corresponding standard deviations for the 100 Hz accumulations.

V. APPLICATION OF INVERSE DIFFRACTION ALGORITHM TO MEASURED DATA

The algorithm of Section III, which uses the phase-screen model of Section II, has been applied to the dual-frequency I and Q scintillation data that are described in Section IV. A number of optimal estimation runs have been made, but most of them had to be discarded due to the discovery of a sign error in one of the underlying model equations. Although the erroneous term is small and does not have large effect, the only results that are presented are those that are completely consistent with the models that have been derived in Section II. This restriction, the slowness of the computations, and this paper's publication deadline left the project with only one good case that was ready for discussion at the time of this writing. Nevertheless, this case offers encouraging results, and therefore, it is worthy of discussion.

A. Results for One Estimation Case

Consider the run whose results are presented in Figs. 4-6. Figure 4 presents three versions of scintillating phase time histories $\phi_s(t)$ at each of the two GPS frequencies. The L2C phase time histories are artificially offset below the L1 time histories in order to avoid confusion on the plot. Figure 5 presents the corresponding plots of the $A_s(t)$ scintillating amplitude times histories of the I and Q accumulations. These amplitudes have been normalized by the average values of the data amplitudes and then offset by +0.5 for the L1 signals and by -0.5 for the L2 signals. Figure 6 presents two estimates of the underlying $VTEC(x)$ vs. x distribution that gave rise to the measured scintillation. The line types of the curves on Figs. 4 and 5 are the same. The green dotted curves are the initial estimates as computed using the method described at the end of Section III, the solid blue curves are the data taken directly from the measured accumulations, and the red dash-dotted curves are the optimal estimates. The line types of the two curves on Fig. 6 are related. The green dotted curve gives the standard quiescent ionosphere value as computed using Eqs. (37) and (38), and the red dash-dotted curve gives the optimal cubic spline estimate of $VTEC(x)$ vs. x. Thus, the green dotted curve has been used to generate the first guess of the splined estimate.

The following parameters characterize various x spacings that have been used to generate Figs. 4-6: The spline grid spacing is δx_c = 171 m and there are N_c = 326 regular cubic spline intervals, which cover a range of 55.746 km. The minimum and maximum $x_{pv}(t_l)$ convected ionospheric LOS pierce points cover a range of 41.804 km. The spline extends 6.971 km past either end of these data points. The respective average and maximum intervals between pierce points, $x_{pv}(t_{l+1}) - x_{pv}(t_l)$, are 70 m and 76 m. The number of FFT points is $N = 2^{15} = 32768$, and the FFT grid spacing is δx = 7.805 m. The FFT periodicity is $N\delta x$ = 255.746 km, and the FFT interval extends 100 km beyond either end of the central $VTEC(x)$ vs. x cubic spline grid. The region of splined periodicity-preserving variations at the lower and upper ends of the FFT interval, as shown at either end of the plot in Fig. 3, has a length of δx_{per} = 6.394 km.

The following *a priori* information has been used in the estimation run associated with Figs. 4-6. The *a priori* altitude, tilt angle, and drift velocity are: h_{nom} = 350 km, $\gamma_{nom} = 0^o$, and v_{nom} = 170 m/sec. The associated *a priori* standard deviations are σ_h = 10 km, $\sigma_\gamma = 5^o$, and σ_v = 30 m/sec. The spline smoothness *a priori* standard deviations are $\sigma_{V'''} = 4.77\times10^8$ electrons/m^5 and $\sigma_{\Delta V''} = 8.79\times10^9$ electrons/m^4. The *a priori* mean $VTEC$, which is based on the Klobuchar broadcast model that was valid at the time of the observations [15], is $\overline{V}_{nom} = 12.998\times10^{16}$ electrons/m^2, and its standard deviation is $\sigma_{\overline{V}} = 1\times10^{16}$ electrons/m^2. As defined in Eqs. (27) and (29), the full w_i''' and w_i'' weights for these smoothness penalties apply for the outer $N_{w23}\delta x_c$ = 4.617 km of the regular spline interval, and the neighboring regions where the weights decay linearly to zero have length $\Delta N_{w23}\delta x_c$ = 1.197 km. The $\Delta\tau_{\rho na}$ common-mode phase slop polynomial in Eq. (20) has order T = 16, and its associated *a priori* RMS value is $\sigma_{\Delta\tau} = 1.987\times10^{-10}$ sec. The ΔG_{L1} and ΔG_{L2} gain variation slop polynomials in Eqs. (19a) and (19b) have order M = 6, and their associated *a priori* RMS slopes are $\sigma_{\Delta G'}$ = 0.100 dB/sec.

Altogether there are 687 unknown elements in the X vector for the estimation problem associated with Figs. 4-6. There are 599 dual-frequency I/Q data samples, which translates into $4\times599 = 2396$ independent measurements. Thus, the estimation problem is over-determined as it should be.

The optimal solutions as shown by the red dash-dotted curves have been computed using 11 Levenberg-Marquardt iterations. These iterations took a total of about 48 hours to complete when run in MATLAB on one core of a 3 GHz Windows XP workstation.

If one compares the phase and amplitude fits to the data in Figs. 4 and 5, one finds that they are both better for the optimal estimate than for the initial estimate, i.e., the first guess. This is fairly obvious for the amplitude plots on Fig. 5: Notice how virtually every spike on a blue curve has a corresponding spike on the associated red curve of nearly equal magnitude while the green curve can have spikes in odd places or with the wrong magnitude. One

can see this same trend on Fig. 4, but the differences between the green, red, and blue curves seem less pronounced. In truth, the levels of the optimal and the first-guess fit errors on Fig. 4 are roughly commensurate with the levels on Fig. 5. In order to see this, note that a relative amplitude error of 0.25 on Fig. 5, which seems large on that figure, is comparable to a phase error of only $0.25/(2\pi) = 0.040$ cycles on Fig. 4. An error of only 0.040 cycles is deceptively small relative to the large low-frequency phase variations that occur on Fig. 4.

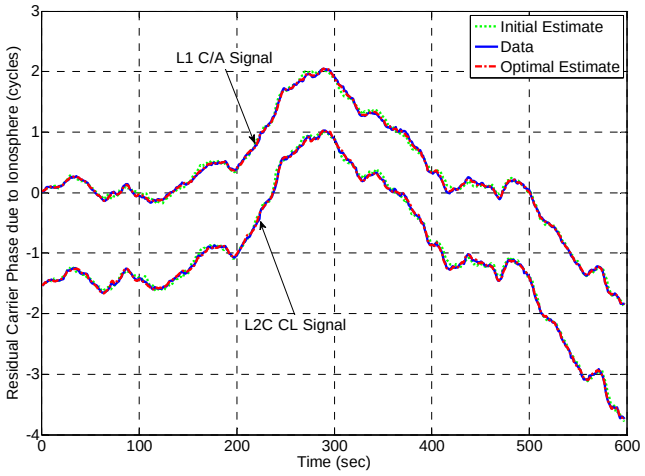

Fig. 4. Carrier phase time histories for scintillating L1 C/A and L2C CL signals.

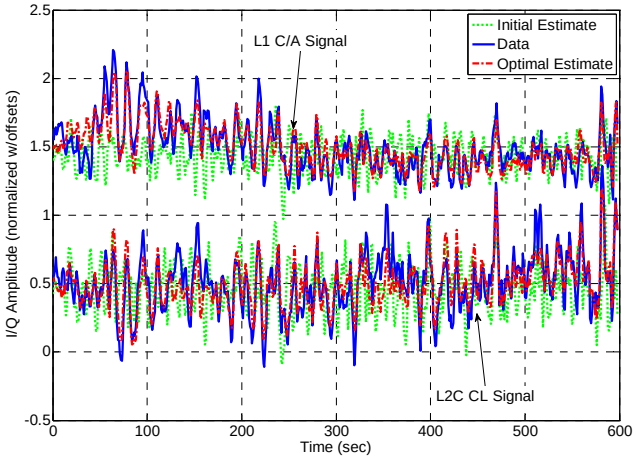

Fig. 5. Accumulation amplitude time histories for scintillating L1 C/A and L2C CL signals.

The improvement of the optimal fit can be quantified: The RMS error between the optimal modeled L1 *I* and *Q* accumulations and the L1 accumulation data is 3.0 times smaller than the RMS error between the data and the L1 accumulations that are calculated based on the first guess of *X*. Similarly, the optimal estimate of *X* produces modeled L2 accumulations that fit the L2 data with an RMS error that is 2.6 times smaller than the corresponding RMS error for the initial guess of *X*.

Note that the increased level of improvement for the L1 signal probably is the result of the optimal solution's ability to model the low-frequency amplitude hump that occurs between t = 50 sec and t = 200 sec. This ability comes from the gain perturbation model in Eqs. (19a) and (19b), which is sensible given that this hump is likely the result multi-path or antenna gain variation, not of scintillation.

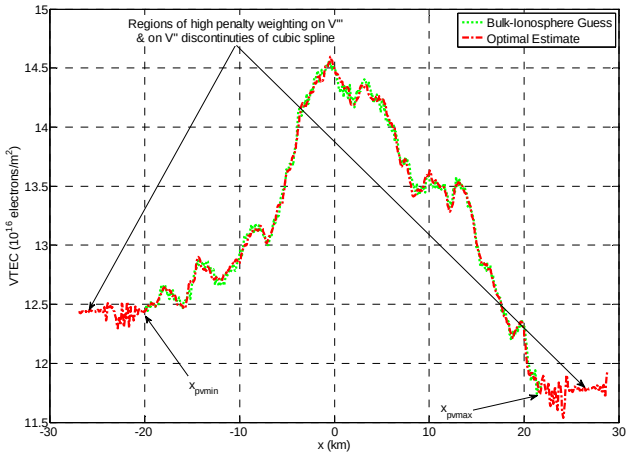

Fig. 6. Initial guess and optimal estimate of "frozen", drifting VTEC(x) vs. x distribution.

The improved fit of the optimal amplitude and phase curves is remarkable. The L1 and L2 fit improvements result from an identical estimate of the *VTEC*(x) vs. x profile, the one shown as the red dash-dotted curve in Fig. 6. This result implies that the physics embodied in the phase-screen model and in the Huygens-Fresnel integral have the power to describe actual scintillation data. Also remarkable are the significant differences in the green and red phase and amplitude estimates of Figs. 4 and 5 that are caused by small differences in the corresponding *VTEC*(x) vs. x distributions of Fig. 6.

B. Questions about Estimation Results

Although the optimal estimate shows significant improvements in its dual-frequency amplitude and phase fits, several aspects of its solution give cause for concern. First, the RMS errors between the red dash-dotted optimal estimate curves of Figs. 4 and 5 and the corresponding blue data curves are about 8-13 times larger than they would be if the differences were due purely to random measurement error. This fact suggests that there is some sort of modeling error. The power spectra of the measurement residuals, which are defined to be the differences between the measured and modeled accumulations, do not reveal any obvious frequency structure of the modeling error.

Any one of several modeling assumptions may have given rise to the observed discrepancy in the power of the residual errors. The assumption of a "frozen", west-to-

east-drifting $VTEC(x)$ vs. x distribution may cause some of the systematic error as may the assumption of a constant drift velocity. The assumption of a constant ionospheric altitude may cause additional error. Another possible source of error is the assumption of a thin phase screen rather than an ionosphere with finite thickness. Unfortunately, the availability of data from only a single receiver limits the type of physical model that can be used while maintaining observability of the unknown model parameters in the estimated X vector.

In the future, it is planned to collect data using an array of receivers. This type of data collection campaign will allow some of these restrictive assumptions to be relaxed. It is hoped that such an approach will eventually lead to better fits to the observed data.

Another unusual feature of the optimal estimate is the presence of high-frequency variations of $VTEC(x)$ vs. x in the regions -24 km < x < -21 km and 21.5 km < x < 24 km. These are evident in the red dash-dotted curve of Fig. 6. These variations appear to be unphysical. They lie outside the region of $x_{pv}(t_l)$ data points, as indicated on the figure. Less obvious, however, is the fact that these variations lie within the central region of zero w_i''' and w_i'' weightings in the *a priori* penalty terms of Eqs. (26) and (28). These penalty terms have been specifically designed in order to avoid such un-physical estimates in regions where the $VTEC(x)$ vs. x distribution is not adequately constrained by the accumulation data. It appears, therefore, that the regions of non-zero w_i''' and w_i'' weightings need to be extended towards the center of the spline through an increase of N_{w23} or ΔN_{w23}.

C. The Problem of Altitude, Tilt, and Drift Velocity Estimation

A significant concern about the estimator is its ability to determine the ionospheric altitude, h, tilt angle, γ, and drift velocity, v. The optimal estimates of these quantities differ from their initial guesses only by small increments. The initial and optimal altitude estimates are, respectively, 350 km and 349.995 km. For tilt angle the initial and optimal estimates are 0^o and -0.0074^o and for ionospheric drift velocity they are 170 m/sec and 170.0077 m/sec. The corresponding computed estimation error standard deviations from the Eq. (36) P_{XX} covariance matrix are 0.756 km for altitude, 0.0693^o for tilt angle, and 0.1059 m/sec for drift rate. Each of these *a posteriori* standard deviations are at least an order of magnitude smaller than the *a priori* values of σ_h (10 km), σ_γ (5^o), and σ_v (30 m/sec) that have been used in the corresponding Eq. (32) penalty terms. It is unlikely that the estimator would be able to determine these three quantities to the high levels of precision indicated by their computed *a posteriori* standard deviations without modifying them from their initial guessed values. One normally cannot make such good first guesses of estimated quantities.

These counter-intuitive results may be explainable in terms of nonlinear estimation. Perhaps the nonlinearities in the phase-screen model of Section II lead to the existence of multiple local minima of the squared-error cost function $J(X)$. Perhaps the estimates discussed above lie near a local minimum that is not the global minimum, i.e., that is not truly the optimal estimate. Such a situation might also help to explain the relative poorness of the fits in Figs. 4 and 5 relative to the RMS level of the random errors in the accumulation measurements.

The possibility of multiple local minima has been investigated by starting the optimal estimation algorithm from a variety of first guesses of h, γ, and v. The cases that have been considered lie on a 3-dimensional grid in (h, γ, v) space. The altitude guess grid values are 300, 325, 350, 375, and 400 km. The tilt angle grid values are -5, 0, and +5 deg. The drift velocity grid values are 110, 135, 160, and 185 m/sec. Altogether, 60 distinct first-guess combinations of h, γ, and v have been tried. This use of many different first guesses in the optimization algorithm represents a "brute-force" attempt to deal with the possibility of multiple local minima. Unfortunately, these results are not completely reliable because they contain the sign error that has been mentioned at the beginning of this section. Nevertheless, because the effect of the sign error is not large, tentative conclusions may be drawn from these results.

These tentative results indicate that the altitude and tilt angle have very weak observability for the case of a single receiver, but the drift velocity observability is not quite as weak. Strong observability corresponds to there being a well-defined minimum with respect to the quantity in question.

Another tentative indication of these results is that there can be multiple local minima. At the highest 2 altitudes, there were 2 distinct local cost minima with respect to γ and v.

A very puzzling aspect of these preliminary results has to do with the low levels of curvature on plots of J versus these 3 variables. These low levels of curvature give rise to the indistinctness of the minima and the corresponding weak observability of h and γ and moderate observability of v. As an example, the computed *a posteriori* estimation error standard deviation of h should be roughly proportional to $1/\sqrt{d^2J/dh^2}$, which represents a scalar version of the generalization of Eq. (36) to the case of a general negative-log-probability-density cost function. Therefore, the low standard deviations of h, γ, and v as computed based on P_{XX} from Eq. (36) imply that the cost

variations found in the present study should have far more curvature than they do and that the cost function should have very distinct local minima.

It is unclear why there is a large discrepancy between the curvature of the cost contours found in this preliminary study and the inverse of the P_{XX} covariance matrix of Eq. (36). There are several possible explanations. One is that a finer scale of sampling needs to be performed in this type of study in order to see the high curvature. This possibility rests on the idea that there may be many local minima in a jagged cost contour that can have a locally large curvature even though its "averaged" curvature may be low.

An alternative possibility is that the P_{XX} from Eq. (36) is misleading. It is based on a linear approximation of the underlying measurement model equations. This linearization neglects a quadratic term in the computation of the true P_{XX}. Often this quadratic term is insignificant. If it is significant, however, then consideration of this term may resolve the paradox. It is planned to investigate these issues via further research.

VI. SUMMARY AND CONCLUSIONS

A method of inverse diffraction has been developed as a means for estimating the variations of the vertical total electron content distributions that give rise to equatorial ionospheric scintillation. These estimates are made based on in-phase and quadrature accumulation data that have been collected using a dual-frequency GPS receiver. The inverse diffraction algorithm is based on a diffraction model that uses a phase-screen approximation and a modified Huygens-Fresnel integral, one that accounts for non-normal incidence of the diffracted wave on the phase-screen plane. This model computes the effects of 1-dimensional fine-scale electron density variations on the received amplitudes and phases of GPS signals. The relevant direction of the electron density variations is the east-west direction as measured relative to the local magnetic field. This model makes several simplifying assumptions that are deemed necessary in order to maintain problem observability when using data from the line of sight between a single receiver and a single GPS satellite. The diffraction model is inverted using standard nonlinear least-squares techniques. These techniques start from an initial guess based on a bulk ionosphere model, and they perform gradient-based iterations that improve the fit between the modeled and measured accumulations.

The new algorithm has been applied to dual-frequency GPS data that have been collected in Brazil during a time of weak scintillation. The scintillation intensity reached an S_4 value of 0.4 on the L1 C/A signal and a value of 0.5 on the new L2C CL signal. The estimation algorithm decreased the RMS values of its residual measurement errors by factors of 3 and 2.6, respectively, for the L1 and L2 signals. The resulting fits clearly show that the phase-screen approximation and the Huygens-Fresnel integral provide an ability to model the effects at multiple transmission frequencies of actual weak scintillation. Despite this success, the inverse diffraction results contain several puzzling features. These features require further investigation before full confidence can be placed in this new method's ability to image fine-scale electron density variations in the disturbed, scintillating ionosphere.

ACKNOWLEDGEMENT

This work has been supported in part by the NSF through grant Nos. ATM-0720209 and ATM-0719872. Cassandra G. Fesen is the monitor for both grants.

REFERENCES

1. Humphreys, T.E., Ledvina, B.M., Psiaki, M.L., and Kintner, P.M. Jr., "Analysis of Ionospheric Scintillations Using Wideband GPS L1 C/A Signal Data," *Proc. ION GNSS 2004*, Long Beach, CA, Sept. 21-24, 2004, pp. 399-407.
2. Aarons, J., "Global Morphology of Ionospheric Scintillations," *Proc. of the IEEE*, 70(4), 1982, pp. 360-378.
3. Humphreys, T.E., Psiaki, M.L., Kintner, P.M. Jr., and Ledvina, B.M., "GPS Carrier Tracking Loop Performance in the presence of Ionospheric Scintillations," *Proc. ION GNSS 2005*, Long Beach, CA, Sept. 13-16, 2005, pp. 156-167.
4. Humphreys, T.E., Psiaki, M.L., Ledvina, B.M., Cerruti, A.P., and Kintner, P.M., "A Data-Driven Simulation Testbed for Evaluating GPS Carrier Tracking Loops in Severe Ionospheric Scintillation," to appear in *IEEE Trans. on Aerospace and Electronic Systems*.
5. Keskinen, M.J., Ossakow, S.L., and Fejer, B.G., "Three-Dimensional Nonlinear Evolution of Equatorial Ionospheric Spread-F Bubbles," *Geophysical Research Letters*, 30(16), Article. No. 1855, 2003.
6. Yeh, K.C., and Liu, C.-H., "Radio Wave Scintillations in the Ionosphere," *Proc. of the IEEE*, 70, 324-360, 1982.
7. Rino, C.L., and Fremouw, E.J., "The Angle Dependence of Singly Scattered Wave-Fields," *Journal of Atmospheric and Terrestrial Physics*, 39(8), 859-868, 1977.
8. Rino, C.L., "A Power Law Phase Screen Model for Ionospheric Scintillation, 1, Weak Scatter," *Radio Science*, 14(6), 1135-1145, 1979.
9. Rino, C.L., "A Power Law Phase Screen Model for Ionospheric Scintillation, 2, Strong Scatter," *Radio Science*, 14(6), 1147-1155, 1979.

10. Psiaki, M.L., Humphreys, T.E., Cerruti, A.P., Powell, S.P., and Kintner, P.M. Jr., "Tracking L1 C/A and L2C Signals through Ionospheric Scintillations," *Proc. ION GNSS 2007*, Fort Worth, TX, Sept. 25-28, 2007, pp. 246-268.
11. Pidwerbetsky, A.P., "Simulation and Analysis of Wave Propagation through Random Media," Cornell University Ph.D. Thesis in Applied and Engineering Physics, pp. 17-18, 1988.
12. Mohiuddin, S., Humphreys, T.E., and Psiaki, M.L., "A Technique for Determining the Carrier Phase Differences between Independent GPS Receivers during Scintillation," *Proc. ION GNSS 2007*, Fort Worth, TX, Sept. 25-28, 2007, pp. 1651-1660.
13. Kintner, P.M., Ledvina, B.M., de Paula, E.R., and Kantor, I.J., "The Size, Shape, Orientation, Speed, and Duration of GPS Equatorial Anomaly Scintillations," *Radio Science*, 39(2), Art. No. RS2012, 2004.
14. Ledvina, B.M., Psiaki, M.L., Kintner, P.M., and de Paula, E.R., "Scattering Altitude Estimation Using Closely-Spaced GPS Receivers" *Proc. 11th International Ionospheric Effects Symposium*, Alexandria, VA, May 3-5, 2005.
15. Klobuchar, J.A., "Ionospheric Effects on GPS," in *Global Positioning System: Theory and Applications, Vol. I*, Parkinson, B.W., and Spilker, J.J. Jr., eds., American Institute of Aeronautics and Astronautics, (Washington, 1996), pp. 485-515.
16. Lipson, S.G., Lipson, H., and Tannhauser, D.S., *Optical Physics, 3rd Ed.*, Cambridge Univ. Press, (Cambridge, UK, 1995), pp. 156-158.
17. Gill, P.E., Murray, W., and Wright, M.H., *Practical Optimization*, Academic Press, (New York, 1981), pp. 37-40, 133-141.
18. Bar-Shalom, Y., Li, X.-R., and Kirubarajan, T., *Estimation with Applications to Tracking and Navigation*, J. Wiley & Sons, (New York, 2001), pp. 236-240.
19. Montenbruck, O., and Gill, E., *Satellite Orbits*, Springer, (New York, 2005), pp. 221-224.